

Effects of dark matter self-interaction on the evolution of the Sagittarius stream

Connor Hainje

Advised by Professor Mariangela Lisanti

April 30, 2021

Abstract

I present a novel test of self-interacting dark matter (SIDM) models by analyzing the impact of self-interaction on the infall of the Sagittarius (Sgr) dwarf spheroidal galaxy. A review of the history of dark matter evidence and the development of the Λ CDM cosmological model is included, followed by a review of the motivations for and viability of SIDM models. Sgr is then presented as a testbed for these models, since its unique orbital history is highly sensitive to the microphysics determining the Galactic gravitational potential. I present three simulations of the Sgr infall: two using collisionless dark matter with cuspy and cored initial galactic profiles, and one using self-interacting dark matter. It is found that the inclusion of dark matter self-interaction has profound impacts on the resulting shape and distribution of the Sgr stream. In particular, we find that the distribution of radial velocities is impacted substantially, with the SIDM merger unable to reconcile both the shape of the stream and the observed radial velocity of the progenitor.

This paper represents my own work in accordance with University regulations.

/s/ Connor Hainje

Contents

1	Introduction	1
1.1	Evidence for dark matter	1
1.2	Lambda-CDM	3
1.3	Structure formation	6
1.4	Small-scale problems	8
2	Self-interacting dark matter	12
2.1	Introduction	12
2.2	Particle physics models	14
2.2.1	Self-coupled scalar	14
2.2.2	Light mediator	16
2.2.3	Strong interactions	17
2.3	Analytic description of mass distributions	19
2.4	Self-interaction in simulation	25
3	Sagittarius	29
3.1	Overview	29
3.2	Modern models	32
4	Simulation setup	37
4.1	Pipeline and parameters	37
4.2	Equilibration	40
5	Full infall simulations	47
5.1	Description and initial results	47
5.2	Identifying the Sgr progenitor	51
5.3	Comparison to stream data	58
5.3.1	Progenitor coordinates	58

CONTENTS	iii
5.3.2 Stream shape	62
5.3.3 2MASS M-giants	65
6 Conclusions	69
Acknowledgements	72
Institutional acknowledgements	73

Chapter 1

Introduction

1.1 Evidence for dark matter

In 1932, Jan Oort studied the velocities of stars near the Sun, and he found that the velocities of these stars were systematically larger than expected [1]. From the velocities of stars at a given radius in a galaxy, one can measure the gravitational mass of all objects inside that radius. As such, Oort's velocity findings were really a statement about the mass of the Milky Way. In Oort's own words, these velocities implied that the amount of gravitating matter in the Milky Way must be larger than what one can estimate by simply counting stars, with the latter falling short by roughly 30-50% [2].

The next year, Fritz Zwicky studied velocity dispersions in the Coma galaxy cluster [3, 4]. From his measurements, he found that the velocity dispersions required “10 to 100 times more mass” for the cluster to remain bound than could be accounted for by luminous matter. He concluded that there must be some large source of non-luminous matter present to account for the difference, calling the non-luminous matter “dunkle Materie”, or “dark matter”. This is often cited as the origin of the term.

Over the next few decades, evidence continued to mount for the existence of dark matter. Rotation curves began being considered, first by Babcock in 1939 [5] and Oort in 1940 [6]. In the words of Oort, “the distribution of mass in this object [the M31 galaxy] appears to bear almost no resemblance to that of light.” Studies of globular clusters in the Milky Way indicated that at least two-to-three times as much mass must lie outside the orbit of the Sun as inside [7]. Studies of binary galaxies revealed large mass-to-light ratios [8, 9]. More galaxy clusters were studied, and the trends noted by Zwicky were found to hold generally [10]. This mounting evidence largely took the form of acknowledgement of a large mass-to-light ratio; it was not widely thought that a yet unknown form of matter was responsible.

By the 1970s, however, that would change. This was in large part due to developments on a few different fronts. First, the 1960s and 70s saw new methods for measuring the masses of galaxy clusters. Both X-ray measurements and gravitational lensing first began being used in the 1960s to obtain measurements of the masses of galaxy clusters [10]. These studies independently confirmed the large, non-luminous masses that were indicated by the previous velocity analyses.

Second, the cosmic microwave background was discovered in 1965 [11, 12], and found to be remarkably isotropic (to better than a part in 10^4). However, strictly baryonic models of the universe suggest anisotropies in the CMB on the order of $\sim 3 \times 10^{-4}$. If the Universe contained some non-baryonic matter which interacted with photons only gravitationally, however, the predicted anisotropies are revised downward, closer to 10^{-5} , consistent with observation. Dark matter seems to fit this role perfectly. Anisotropies on this scale have been observed by more recent studies, beginning with the COBE satellite in 1992 [13, 14] and more recently with the WMAP [15] and Planck [16] missions.

Third, data from rotation curves became quite convincing. Rubin and Ford

published improved optical data from the galaxy M31, the same galaxy studied by Oort in 1940 [17]. They found that, to even farther radii than had been previously considered, the rotation curve did *not* decrease outside the optically bright region of the galaxy, an even stronger indicator of the existence of mass not accounted for by luminous matter. Similarly, Roberts and Rots [18] and Roberts and Whitehurst [19] used measurements of 21cm hydrogen emissions to draw very similar conclusions.

Lastly, 1974 saw two watershed papers by independent research groups, each concluding that galaxies have dark halos. Einasto, Kaasik, and Saar wrote “the mass of galactic coronae halos exceeds the mass of populations of known stars by one order of magnitude, as do the effective dimensions” [20]. Similarly, Ostriker, Peebles, and Yahil wrote “the very large mass-to-light ratio and the very great extent of the spiral galaxies can perhaps most plausibly be understood as due to a giant halo of faint stars” [21]. They also note that the year prior, Ostriker and Peebles had come to a similar conclusion from considerations of stability, finding the traditional disk galaxy model to be unstable without a spherical halo [22].

1.2 Lambda-CDM

Since these discoveries, it has been widely believed among astronomers and cosmologists that non-baryonic dark matter exists, that it comprises large, spherical halos around galaxies, and that it played an integral role in the formation of the structures we can see today. Evidence has become increasingly strong with improved measurements of the anisotropy in the CMB (such as the COBE experiment mentioned above), as well as better measurements of the masses of various structures thanks to improved rotation curves and better X-ray and gravitational lensing instrumentation.

Another major question of the twentieth century which came to be largely

settled toward its end was that of the cosmological constant, Λ . This constant was introduced by Einstein into his theory of general relativity as a means to achieve a static universe, though today it is used to describe the accelerating expansion of the universe. Physically, this constant can be interpreted as the vacuum energy density of empty space. It is often called “dark energy” for this reason [23]. In the late 1990s, measurements of Type Ia supernovae strongly constrained Λ to be positive, giving empty space a significant, constant vacuum energy [24, 25].

These findings, combined with large amounts of evidence for the Big Bang hypothesis, are all most simply described by the Λ CDM model, sometimes called the standard model of cosmology or the concordance model [26]. The model describes the Universe as consisting of three components—the cosmological constant Λ , cold dark matter (CDM), and standard matter—operating under general relativity and coming from an origination event roughly 14 Gyr ago (the Big Bang). This rather simple model is remarkably successful at explaining the Universe.

Through its inclusion of the Big Bang event, the Λ CDM model gives an explanation for the origin of the CMB. In this model, the CMB is a residual radiation left-over from a period shortly after the Big Bang, where the Universe was hot ($>10,000$ K). As the Universe cooled and structures began to form, the photons from this period began to propagate freely in all directions.

The Λ CDM model also provides a well-tested account of the formation of structures in the Universe [26]. In the early Universe, small gravitational perturbations caused matter to collapse into small structures. These small structures—effectively perturbations in the mass density of the Universe—created gravitational potential wells, attracting other small structures and assembling together to produce larger ones. This works especially well for describing the distribution of dark matter in the Universe, as small pockets of

dark matter converge to form subhalos, halos, and larger. The case for baryonic matter and galaxy formation is more complicated, involving baryonic processes, gas dynamics, and more, but is also well-explained in the régime of hierarchical structure formation. Simulations of hierarchical structure formation have found that it is able to account well for the observed distribution of structures on the scales of galaxies, galaxy clusters, and larger. The implications of this model of structure formation are considered in more detail in the next section.

In fact, the success of this theory of structure formation serves as reason to believe that dark matter is cold (hence the “C” in Λ CDM). Dark matter being “cold” means that it was non-relativistic at the time of decoupling (the period in the early Universe when matter began to fall out of thermal equilibrium) [27]. By contrast, “hot” dark matter (HDM) would have been relativistic at the time of decoupling. Given these higher velocities, the velocity dispersion of HDM would have been non-negligible (differing from the negligible velocity dispersion of CDM). A finite velocity dispersion, however, would have prevented the dark matter particles from being bound to shallow gravitational potential wells, further preventing the formation of small-scale structures [23]. Thus, HDM fails to form structure.

On its own, Λ CDM is remarkably able to explain most of our observations of the Universe. However, there are a few cosmological problems which have arisen. One is known as the horizon problem [23, 28], which points out the the CMB is, to a high degree, isotropic, indicating that the photons making up this radiation are roughly in thermal equilibrium across the sky. However, this means that regions of the sky which are too far separated to be causally connected have remained in equilibrium. This is not explained by Λ CDM.

Another problem is the flatness problem, which points out that there is potentially a fine-tuning problem with the vanilla Λ CDM model [23, 28]. The

Universe as we observe it is approximately flat today, meaning that its curvature is approximately unity. If the curvature were not unity, its deviation from flatness is expected to grow with time. As such, if the Universe is not flat, it must have been *very* close to unity at early times, meaning that this parameter may need to be “fine-tuned” to achieve a reasonable explanation. The problem is that our model should be able to describe parameters like these *without* fine-tuning.

Combining the Λ CDM model with the theory of cosmic inflation, however, solves both of these problems [28]. Inflation posits that the Big Bang was followed by a period of rapid (exponential!) inflationary expansion. Such a phenomenon would solve the horizon problem, as the whole observable Universe would have originated from a much smaller, thermally-connected region before inflation. It also solves the flatness problem, as inflation would have significantly stretched and flattened any curvature in the Universe, providing a natural explanation for the observed flatness today. In fact, this creates a sort of inverse fine-tuning problem: in this theory, any curvature which is *far* from unity requires fine-tuning.

1.3 Structure formation

As stated above, the Λ CDM model predicts structures to form in the Universe as a result of gravitational perturbations at early times. As expansion slows, the pockets of matter created by these perturbations host small gravitational potential wells, causing nearby matter to collapse inward and the growth of structure to occur. With the majority of matter in the Universe being dark matter, the first structures which occur are small dark matter halos. The halos observable today are the result of the hierarchical combination of these smaller halos.

The abundance of these halos can be described by extended Press-Schechter

(EPS) theory [29]. This theory is grounded on rather simple assumptions: that one can use a spherical collapse model and that one can extrapolate from linear perturbation theory even into non-linear régimes. Despite these assumptions, it has been shown to give predictions about the mass spectrum of dark matter halos which are in accord with high-resolution numerical simulations.

The halos themselves can be described as virialized objects with mass

$$M_{\text{vir}} = \frac{4\pi}{3} R_{\text{vir}}^3 \Delta_c \rho_c, \quad (1.1)$$

where R_{vir} is the virial radius, ρ_c is the critical density of the Universe, and Δ_c is the over-density parameter. As noted in [29], identifying the mass of a halo requires a way of defining the outer edge, or the radius, of the halo, and this is done by a choice of Δ_c . It is often chosen to match the expected over-density for dark matter in a region which has undergone an idealized spherical collapse. Such values are often on the order of $\mathcal{O}(100)$; in this work, we choose to follow a common convention by setting $\Delta_c = 200$. We thus mark the virial mass and radius with a subscript 200 instead of “vir”.

The Λ CDM model also provides predictions about the internal structure of these dark matter halos. Dark matter-only N-body simulations were performed as early as 1988 [30], with higher-resolution simulations like [31] and [32] following shortly thereafter. The resulting halos from these simulations were found to agree remarkably well with a *two-power* density profile [33]

$$\rho(r) = \frac{\rho_0}{(r/a)^\alpha (1+r/a)^{\beta-\alpha}}, \quad (1.2)$$

where ρ_0 is a characteristic density for the halo and a is the length scale. Special cases of this model include $(\alpha, \beta) = (1, 4)$, the Hernquist model [34], and $(\alpha, \beta) = (1, 3)$, the NFW model [32, 35]. In general, the NFW model enjoys the most usage as one of the most simple and accurate models of the

mass density distribution of smaller halos.

The required parameters above, ρ_0 and a , are typically reformulated for the NFW distribution. In particular, we can take a given virial mass M_{200} , determine the corresponding virial radius R_{200} , and define the halo concentration $c = R_{200}/a$. The characteristic density can be found by integrating the density profile up to R_{200} and setting it equal to M_{200} . In this way, the virial mass and concentration are enough to completely specify the NFW distribution. The result is given by

$$\rho_0 = \frac{M_{200}}{4\pi a^3 f(c)}, \quad f(c) = \log(1 + c) - c/(1 + c). \quad (1.3)$$

As these halos are formed hierarchically from smaller halos, however, it has been found that the dense centers of the subhalos are able to survive the merging process. A direct result of this finding is that dark matter halos today should be full of substructure with satellite subhalos of varying sizes. In fact, simulations have shown that the number of subhalos within a halo is approximately self-similar for host halo mass [29]. While it is difficult to determine a method for identifying and counting these subhalos, it does yield a testable prediction of the small-scale structure of dark matter in the Λ CDM paradigm.

1.4 Small-scale problems

The theory of structure formation that follows from Λ CDM leads us to a few important results. First, we expect the density distributions of dark matter halos to approximately follow the NFW model, specifically with r^{-1} dependence for small r . Second, we expect rich substructure in massive dark matter halos with predictions for the number of subhalos of varying masses contained within. Third, through galaxy formation and the method

of abundance matching, we obtain predictions about the number and masses of satellite galaxies that should be hosted in galaxies like the Milky Way. These three key deductions form the basis for the three classic **small-scale problems** in the Λ CDM model.

The first problem we will discuss is known as the **core-cusp problem**, which is primarily related to the first deduction above. Dark matter-only simulations of CDM halos show that the expected distribution of mass follows a density distribution that is very dense and *cuspy*, i.e. one that goes like r^{-1} at small radii (Bullock and Boylan-Kolchin 2017). As early as 1993, however, it was pointed out that such a distribution is inconsistent with observational data. In particular, “[cuspy] density profiles are excluded by gravitational lensing analyses on cluster scales and by the rotation curves of gas-rich, halo-dominated dwarf spirals on small scales” [36]. It was also recognized by Navarro, Frenk, and White, who wrote “CDM halos are too concentrated to be consistent with the halo parameters inferred for dwarf irregulars” [32].

The second problem is the **missing satellites** problem. Λ CDM simulations predict that galaxies as large as the Milky Way should have as many as $\sim 10^3$ dark subhalos large enough to host dwarf galaxies [29]. However, as of 2019, less than 60 dwarf galaxies are known within the Milky Way [37].

There exists a potential solution to the missing satellites problem, however, in the form of abundance matching. First, one can expect that dark matter halos become less efficient at making galaxies with decreasing mass, and therefore there exists some threshold mass below which these halos remain completely dark. Then, abundance matching allows one to “solve” the missing satellites problem for the subhalos above this threshold [29].

This solution to the missing satellites problem thus makes a testable prediction. The central masses of Milky Way satellites should be consistent with the central masses of the most massive subhalos in Λ CDM simulation [29].

First probed by Boylan-Kolchin et al. in 2011 [38], however, this does not hold; the most massive subhalos predicted in simulation are significantly more massive than the most massive satellite galaxies. If these subhalos do exist but have just remained dark, then we have a new problem: why did these subhalos fail to form galaxies? This is known as the **too-big-to-fail problem**, as these subhalos ought to be too big to fail to form observable galaxies. If these massive dark subhalos just do not exist, then this is a fundamental failing of the Λ CDM model’s predictions in line with the missing satellites problem.

Some believe that these small-scale problems are the result of the omission of baryonic effects in Λ CDM simulations. As described above, the majority of the conflicting predictions come as the result of dark matter-only simulations. Further, in recent years, it has been shown that all of the above problems (and other small-scale issues) can be reduced or eliminated by the inclusion of stellar feedback and other effects. For example, [39] show that supernova feedback can alleviate the core-cusp problem, and [40] show that stellar feedback can explain the too-big-to-fail problem. These works, however, are subject to their fair share of assumptions.

However, prior to these findings, researchers sought modifications to the model that would preserve the successes of Λ CDM on large scales *and* solve the small-scale problems. Some researchers have sought modifications to the model of gravity, but a more popular avenue has been the modification of the dark matter model. While the integration of more sophisticated baryonic processes may be sufficient to solve the small-scale problems, these studies have not ruled out other proposed dark matter models. Moreover, these alternative models have proved quite fruitful in making available a wide variety of descriptions of the particle nature of dark matter. As such, further tests of Λ CDM and these alternative dark matter models are necessary as probes of dark matter particle physics.

This work is another of these tests. In particular, we consider the *self-interacting dark matter* (SIDM) model, which posits that there may exist a non-gravitational mechanism by which dark matter particles interact with one another. We investigate the viability of this model by studying and simulating the infall of the Sagittarius dwarf spheroidal galaxy, whose orbit has left tidal debris in a spectacular stream which arcs across the sky. The orbital history of Sagittarius is quite sensitive to the specific microphysics which determine the Galactic gravitational potential, so the effects of a new dark matter model may manifest in an observable manner in the resultant stream. To this end, we begin by reviewing the SIDM model in Chapter 2 and the Sagittarius galaxy in Chapter 3. We then discuss the setup of our infall simulations in Chapter 4, before discussing the results in Chapter 5.

Chapter 2

Self-interacting dark matter

2.1 Introduction

Self-interacting dark matter (SIDM) was introduced in 2000 by Spergel and Steinhardt [41]. The model was proposed as a solution to the core-cusp and missing satellites problems, as the addition of self-interactions was thought to have three primary effects on the distribution of dark matter.

1. Self-interactions in regions of high density would cause dark matter particles to come unbound, reducing the density of halos primarily in their center region. This would yield a cored density profile rather than a cuspy one, solving the core-cusp problem.
2. It is also expected that interactions would yield a more isotropic velocity dispersion than seen in CDM as well as erase the typical triaxial ellipticity seen in halo shapes. In other words, SIDM halos should be more spherical, a testable prediction.
3. Through the processes of isotropizing the velocity dispersion and reducing density in core regions, it was also expected that substructure

would be greatly reduced, lowering the number of dwarf galaxies and thereby solving the missing satellites problem.

One other feature of the model is that the dark matter scattering rate is naturally dependent on the dark matter density. This means that one expects the effects of self-interaction to be negligible toward the outermost radii of halos and on larger scales, where Λ CDM predictions are consistent with observations. As such, SIDM is able to successfully preserve the large-scale successes of the Λ CDM model.

Shortly thereafter began a wave of numerical simulations to test these predictions. The results of these simulations were mixed. Some were focused on the evolution of galaxies and found confirmation of the predicted effects (more strongly spherical shape, cored density profile) like [42, 43]. Other simulations, like cluster and cosmological simulations, seemed to show that SIDM would be inconsistent with observation [44–46].

At the same time, constraints on the allowed self-interaction cross section began being compiled, primarily from clusters. Given the lack of knowledge of the mass of dark matter particles, cross section values are generally given as cross section-to-mass ratios, denoted σ/m . We will use the term cross section interchangeably with this. [47] used cluster simulations to limit the allowable cross section to $< 0.1 \text{ cm}^2/\text{g}$. Similarly, gravitational lensing data from the MS 2137-23 cluster was used by [48] to limit the cross section to $< 10^{-25.5} \text{ cm}^2/\text{GeV}$, approximately $0.02 \text{ cm}^2/\text{g}$. These cross sections were far too small to solve the small-scale problems in galaxies, as simulations like [43] suggested the necessary cross section to be in the range 10^{-25} to $10^{-23} \text{ cm}^2/\text{MeV}$ (0.05 to $5 \text{ cm}^2/\text{g}$).

However, more recent simulations with higher resolution, better statistics, and updated algorithms for considering self-interactions have relaxed many of these constraints significantly, improving the viability of the model and once again sparking interest in self-interactions. Examples include [49–52].

These newer, better simulations revised the previous constraints and generally show that cross sections on the order of $\sigma/m \sim 0.1$ to $5\text{ cm}^2/\text{g}$ are viable and consistent with observation. Of particular relevance for this thesis is [49], which put forth a novel method for computing the effects of self-interactions in N-body simulation. See Subsection 2.4 for a discussion of their method.

[53] have distilled the relevant modern observational constraints on the self-interaction cross section into a table. The data are reproduced in Table 2.1. In particular, notice that the data are consistent with a decaying cross section as the velocity scale increases. Specifically, all small-scale data is consistent with a cross section of $\gtrsim 0.5$ to $1\text{ cm}^2/\text{g}$, but larger-scale data is consistent with a cross section which is $\sim 0.1\text{ cm}^2/\text{g}$ or smaller. This rules out any particle models we find with a velocity-independent cross section from being able to solve the small-scale problems. However, such models may serve as good approximations in a régime where the cross section does not vary much.

2.2 Particle physics models

Given that very little is known conclusively about the particle physics nature of dark matter, the introduction of the possibility of self-interactions makes way for a wealth of rich new theories. We will cover a few of the most popularly considered models below.

2.2.1 Self-coupled scalar

The first particle model that we consider is the simplest: a scalar particle, φ , that interacts with itself through a two-to-two coupling. This can be

	σ/m (cm ² /g)	v_{rel} (km/s)	Observation
Cores in spiral galaxies	$\gtrsim 1$	30-200	Rotation curves
TBTF in Milky Way	$\gtrsim 0.6$	50	Stellar dispersion
TBTF in Local Group	$\gtrsim 0.5$	50	Stellar dispersion
Cores in clusters	~ 0.1	1500	Stellar dispersion, lensing
Halo shape/ellipticity	$\lesssim 1$	1300	Cluster lensing surveys
Substructure mergers	$\lesssim 2$	500-4000	DM-galaxy offset
Merging clusters	$\lesssim \text{few}$	2000-4000	Post-merger halo survival

Table 2.1: Observational constraints on the self-interaction cross section of dark matter. All listed observations are derived from sets of multiple systems. “TBTF” is the abbreviation for “too-big-to-fail.” This is an abridged reproduction of the table compiled by [53]. A distinction is made between “positive observations” (above the horizontal rule) and “constraints” (below the horizontal rule) by the original authors. References to the original papers are given therein.

described by the Lagrangian

$$\mathcal{L}_{\text{int}} = -\frac{\lambda}{4!} \varphi^4. \quad (2.1)$$

From the Lagrangian, we can read off the Feynman rule for a four-point intersection to have the matrix element $i\mathcal{M} = -i\lambda$, yielding the two-to-two self-interaction differential cross section

$$\frac{d\sigma}{d\Omega} = \frac{\lambda^2}{64\pi^2(4m^2)}. \quad (2.2)$$

Integrating over the solid angle and dividing by two to account for identical particles gives a total cross section

$$\sigma(\varphi\varphi \rightarrow \varphi\varphi) = \frac{\lambda^2}{128\pi m^2}. \quad (2.3)$$

One can easily see that this cross section does not admit any kind of velocity dependence. Thus, one could make this model consistent for a small subset of scales (e.g. $\sigma/m \sim 1 \text{ cm}^2/\text{g}$ for dwarf galaxy scales), but then it would necessarily fail on other scales. This makes the model viable only for analyses of limited scales where the cross section is not expected to vary greatly, but it is generally infeasible as a solution to the small-scale problems.

2.2.2 Light mediator

Perhaps the simplest model with a theory rich enough to solve all of the observed problems is one wherein dark matter self-interactions are mediated by a light particle. We will consider a model where dark matter is represented by χ and has mass m_χ , and the mediator field is ϕ with mass m_ϕ . This theory works with both scalar and vector mediators, depending on what specific theory one wants to consider. Perhaps the best motivated origin for such a model is one where the dark matter particle is charged under a spontaneously broken $U(1)$ symmetry and the mediator arises as the corresponding gauge boson [53].

Such a model would have an interaction Lagrangian given by

$$\mathcal{L}_{\text{int}} = \begin{cases} g_\chi \bar{\chi} \gamma^\mu \chi \phi_\mu & (\text{vector mediator}), \\ g_\chi \bar{\chi} \chi \phi & (\text{scalar mediator}), \end{cases} \quad (2.4)$$

where we let the coupling constant be g_χ . In the non-relativistic limit, the interaction is well-approximated by the Yukawa potential [54, 55]

$$V(r) = \pm \frac{\alpha_\chi}{r} e^{-m_\phi r}, \quad (2.5)$$

where $\alpha_\chi \equiv g_\chi^2/4\pi$ is the dark fine structure constant. The \pm will be set depending on whether the interaction is attractive or repulsive. For a scalar ϕ , the potential is attractive and the sign is $(-)$. For vector ϕ , the po-

tential is attractive (+) for $\chi\bar{\chi}$ scattering and repulsive (−) for $\chi\chi$ and $\bar{\chi}\bar{\chi}$ scattering.

Using the Yukawa potential, we can obtain the Born differential cross section in the limit that $\alpha_\chi m_\chi / m_\phi \ll 1$ to be [53]

$$\frac{d\sigma}{d\Omega} = \frac{\alpha_\chi^2 m_\chi^2}{\left[m_\chi^2 v_{\text{rel}}^2 (1 - \cos \theta)/2 + m_\phi^2\right]^2}. \quad (2.6)$$

An important implication of this formula is that the mediator mass must be positive, i.e. $m_\phi > 0$. If instead $m_\phi = 0$, we would then find that $d\sigma/d\Omega \propto v_{\text{rel}}^{-4}$, which is far too strong at small velocities to admit a solution which is consistent with observations. A small but nonzero mediator mass m_ϕ , on the other hand, allows us to “soften” this velocity-dependence to admit a more consistent model.

While quite simple, it has been shown in [55] that it is possible for this model to simultaneously accommodate all important observations and solve the small scale problems.

2.2.3 Strong interactions

Some of the richest theories for self-interacting dark matter candidates that one can consider are non-Abelian gauge theories where the dark matter candidates arise as composite bound states. In these theories, the self-interaction manifests as a strong interaction.

The motivation for considering such a model comes from our experience with QCD and the visible sector [56]. For a dark matter model to be a good candidate, it must be stable over the lifetime of the Universe and be neutral under Standard Model phenomena. Further, we desire models in which the particles exhibit strong self-interactions. These are all properties exhibited by particles in the visible sector under QCD, so it makes sense to

consider a similar theory to describe our dark matter candidate. However, we do not necessarily know the gauge group or particle properties of dark matter, leaving us a great freedom to vary the model significantly. Many of the resulting models thus have interesting and unique new physics, though these details are greatly model-dependent.

The primary free parameters of models of this kind are the confinement scale Λ (different from the cosmological constant), and the dark quark mass(es). In the event that our “dark QCD” contains no analogue to electromagnetic/weak interactions, meson-like bound states of the dark quarks could be stable [57]. These mesons can be classified as loosely pion-like, where $m \ll \Lambda$, or quarkonium-like, where $m \gg \Lambda$ [56]. There are several proposed models for each of these scenarios; one of the more well-known is the strongly-interacting massive particle, or SIMP, where the dark matter candidate is pion-like and many non-Abelian theories are possible.

Our non-Abelian model may instead look quite similar to visible QCD, wherein the primary stable bound states are baryonic in nature. In [56], it is noted that the advantage of such models is that “dark matter is automatically sufficiently stable, and no further ultraviolet model-building is needed.” One such dark baryon model is “Stealth Dark Matter,” proposed by the LSD collaboration, which is a scalar dark baryon under a confining $SU(4)$ theory. This theory is named *stealth* dark matter because it is found that the baryons are safe from direct detection, though it does predict a spectrum of lighter meson particles that would be possible to detect at colliders [56].

The third class of candidate particles that has received attention are dark glueballs. Glueballs are bound states of only gluons and are predicted to exist in QCD, but are very difficult to detect. Dark glueballs would then be bound states of dark gluons. Such a model is possible if all the dark fermions in the theory have masses significantly larger than Λ . In this case, glueballs may become stable under an accidental symmetry like baryons, allowing them to

be the primary dark matter candidate.

The observables that could result from the above considerations are as diverse as the models themselves. One aspect of these models that we have not considered is what the interactions with the Standard Model could look like. Some models predict the dark matter candidate to be neutral under Standard Model interactions, but its constituents to be charged. In such a case, the model would have a coupling to the photon, and it would be possible to directly detect the particle. We may also consider the case where our theory predicts fundamental fermions. It is plausible that these fermions would obtain at least part of their mass through a coupling to the Higgs boson, again providing a mechanism by which we could directly detect the particles. Kribs and Neil provide more details of these observables, as well as collider-specific results, in [56].

2.3 Analytic description of mass distributions

The most obvious manifestation of dark matter self-interaction is in its effects on astrophysical mass distributions. As such, an understanding of the particle physics properties of dark matter, like the self-interaction cross section, will require the ability to analytically describe and understand the impact of these properties on astrophysical observables. To this end, we present the Jeans approach, an analytic method for deriving the equilibrium distribution of self-interacting dark matter in the presence of baryons, following closely the work of Kaplinghat et al. [58].

The discussion begins with the time-independent Jeans equation, e.g. Equation 4.209 of [33], which is

$$-\bar{v}_j \frac{\partial(\nu \bar{v}_i)}{\partial r_i} = -\nu \frac{\partial \Phi_{\text{tot}}}{\partial r_j} - \frac{\partial(\nu \sigma_{ij}^2)}{\partial r_j}, \quad (2.7)$$

where ν is the number density of dark matter, $\bar{\mathbf{v}}$ is the mean velocity of dark matter particles, and Φ_{tot} is the total gravitational potential. We assume that the velocity dispersion is a constant σ_0 , and that the time required for dark matter to attain equilibrium through self-scattering is long, which allows us to neglect the self-scattering term (on the left side of the equation). We can also write the equation in terms of the mass density ρ instead of the number density ν , as $\rho \propto \nu$ since each dark matter particle will have the same mass. With these assumptions, the equation becomes

$$\rho \nabla_r \Phi_{\text{tot}}(\mathbf{r}) + \sigma_0^2 \nabla_r \rho(\mathbf{r}) = 0. \quad (2.8)$$

We can divide through by ρ and recognize that $\nabla \rho / \rho = \nabla (\ln \rho)$, yielding

$$\sigma_0^2 \nabla_r (\ln \rho(\mathbf{r})) + \nabla_r \Phi_{\text{tot}}(\mathbf{r}) = 0. \quad (2.9)$$

We then take the derivative of the entire equation. At this point, we can introduce a length scale r_0 and corresponding dimensionless length $\mathbf{x} = \mathbf{r}/r_0$.

$$\sigma_0^2 \nabla_x^2 (\ln \rho(\mathbf{x})) + \nabla_x^2 \Phi_{\text{tot}}(\mathbf{x}) = 0. \quad (2.10)$$

Now we can use Poisson's equation, $\nabla_x^2 \Phi_{\text{tot}}(\mathbf{x}) = r_0^2 \nabla_r^2 \Phi_{\text{tot}}(\mathbf{r}) = 4\pi G r_0^2 \rho_{\text{tot}}(\mathbf{r})$. Letting the dark matter density be ρ and the baryon density be ρ_B , this yields

$$\nabla_x^2 (\ln \rho(\mathbf{x})) + (4\pi G r_0^2 / \sigma_0^2) [\rho_B(\mathbf{x}) + \rho(\mathbf{x})] = 0. \quad (2.11)$$

Now, for convenience, we introduce a function $h(\mathbf{x}) = \ln \rho(\mathbf{x})$ such that $\rho(\mathbf{x}) = \rho_0 \exp(h(\mathbf{x}))$. The result is given by Equation 1 in [58], here

$$\nabla_x^2 h(\mathbf{x}) + (4\pi G r_0^2 / \sigma_0^2) [\rho_B(\mathbf{x}) + \rho_0 \exp(h(\mathbf{x}))] = 0. \quad (2.12)$$

As a simple test of this equation, we can consider the case where baryonic

matter dominates. Then, the $\exp(h)$ term can be neglected, yielding

$$\nabla_x^2 h(\mathbf{x}) + (4\pi G r_0^2 / \sigma_0^2) \rho_B(\mathbf{x}) = 0. \quad (2.13)$$

We use Poisson's equation to rewrite ρ_B in terms of the baryonic gravitational potential Φ_B ,

$$\nabla_x^2 h(\mathbf{x}) + \frac{1}{\sigma_0^2} \nabla_x^2 \Phi_B(\mathbf{x}) = 0. \quad (2.14)$$

Integrating over x gives the solution

$$h(\mathbf{x}) = \frac{1}{\sigma_0^2} (\Phi_B(0) - \Phi_B(\mathbf{x})), \quad (2.15)$$

which corresponds to a dark matter density of

$$\rho(\mathbf{x}) = \rho_0 \exp \left[\frac{1}{\sigma_0^2} (\Phi_B(0) - \Phi_B(\mathbf{x})) \right]. \quad (2.16)$$

The authors then recommend defining the core radius as the radius at which the density is half the initial density, $\rho_0/2$. Such a position would give $h(\mathbf{r}_c) = -\ln 2$, or

$$\Phi_B(0) - \Phi_B(\mathbf{r}_c) = -\sigma_0^2 \ln 2. \quad (2.17)$$

Thus, the core size would depend only on the baryonic potential in the case where it dominates, which follows from these assumptions but stands in marked contrast to observation, where the baryonic contribution does not dominate.

At this point, the authors make the move to consider the spherically symmetric case. To do so, they approximate the Milky Way baryon distribution, ρ_B , by a Hernquist profile whose spherical enclosed mass distribution approximates the true enclosed mass distribution. The Hernquist density profile is given by

$$\rho_B(r) = \frac{\rho_{B0}}{(r/r_0)(1+r/r_0)^3}, \quad (2.18)$$

corresponding to a gravitational potential of

$$\Phi_B(r) = -\frac{GM_B}{r+r_0}, \quad (2.19)$$

where M_B is the total mass of baryons in the Milky Way. The free parameters can be set by finding r_0 and $\Phi_B(0)$ such that the circular velocity $V_B(r_0)^2 = -\Phi_B(0)/4$ matches observation. The authors give $\sqrt{-\Phi_B(0)} = 365$ km/s and $r_0 = 2.7$ kpc to be a good fit. We can thus find the core size by solving

$$-\sigma_0^2 \ln 2 = \Phi_B(0) - \Phi_B(r_c) = \Phi_B(0) \left(1 - \frac{1}{1 + r_c/r_0}\right), \quad (2.20)$$

which gives

$$r_c \approx \frac{r_0 \sigma_0^2 \ln 2}{-\Phi_B(0)} = \frac{r_0 \sigma_0^2 \ln 2}{4V_B(r_0)^2}. \quad (2.21)$$

For a typical value of σ_0 , on the order of 150 km/s, we thus obtain

$$r_c \approx 0.3 \text{ kpc} \left(\frac{r_0}{2.7 \text{ kpc}}\right) \left(\frac{\sigma_0}{150 \text{ km/s}}\right)^2 \left(\frac{183 \text{ km/s}}{V_B(r_0)}\right)^2, \quad (2.22)$$

which is quite small.

Let's continue under the assumption that the Milky Way is spherically symmetric and that its baryon profile can be approximated by a Hernquist profile, but drop the assumption that baryons dominate the potential. To begin, we will rewrite the Jeans equation in a spherically symmetric system. First, note that

$$\frac{4\pi G r_0^2}{\sigma_0^2} \rho_B(x) = \frac{1}{\sigma_0^2} \nabla_x^2 \Phi_B(x) = \nabla_x^2 \left(\frac{\Phi_B(0)}{\sigma_0^2} \frac{1}{1+x}\right). \quad (2.23)$$

Thus, we can rewrite the Jeans equation as

$$0 = \nabla_x^2 \left(h(x) + \frac{\Phi_B(0)}{\sigma_0^2} \frac{1}{1+x} \right) + \frac{4\pi G \rho_0 r_0^2}{\sigma_0^2} e^{h(x)} \quad (2.24)$$

$$= \frac{1}{x^2} \frac{\partial}{\partial x} \left[x^2 \frac{\partial}{\partial x} \left(h(x) + \frac{\Phi_B(0)}{\sigma_0^2} \frac{1}{1+x} \right) \right] + \frac{4\pi G \rho_0 r_0^2}{\sigma_0^2} e^{h(x)}. \quad (2.25)$$

We now introduce a new dimensionless variable, $y = x/(1+x)$. Substituting it in yields

$$\frac{(1-y)^4}{y^2} \frac{\partial}{\partial y} \left[y^2 \frac{\partial}{\partial y} \left(h(y) + \frac{\Phi_B(0)}{\sigma_0^2} (1-y) \right) \right] + \frac{4\pi G \rho_0 r_0^2}{\sigma_0^2} e^{h(y)} = 0. \quad (2.26)$$

Simplifying, we then obtain

$$\frac{1}{y^2} \frac{\partial}{\partial y} \left(y^2 \frac{\partial h}{\partial y} \right) - \frac{2\Phi_B(0)}{\sigma_0^2} \frac{1}{y} + \frac{4\pi G \rho_0 r_0^2}{\sigma_0^2} \frac{e^{h(y)}}{(1-y)^4} = 0. \quad (2.27)$$

The authors recommend that this equation be simplified by letting a_0 be the coefficient for the $\exp(h(y))$ term and $a_1 = -\Phi_B(0)/\sigma_0^2$. The boundary conditions imposed on the equation are then $h(0) = 0$ and $h'(0) = -a_1$, which enforce a core in the center.

We can then solve this equation approximately within the core by approximating the third term by a_0 , equivalent to setting $y = 0$ in this term alone. The resulting equation has approximate solution

$$h(y) \approx -a_1 y - \frac{1}{6} a_0 y^2. \quad (2.28)$$

In the case that baryons dominate, $a_1 \gg a_0$ and the y^2 term becomes negligible. The core radius then is given by the solution to

$$\frac{\ln 2}{a_1} = \frac{r_c}{r_0 + r_c}, \quad (2.29)$$

which is

$$r_c = r_0 \frac{\ln 2}{a_1 - \ln 2} \approx \frac{r_0 \sigma_0^2 \ln 2}{-\Phi_B(0)}, \quad (2.30)$$

the same result as we derived before. In the case that dark matter dominates, $a_0 \gg a_1$ and the y term becomes negligible. The core radius is given by the solution to

$$\frac{6 \ln 2}{a_0} = \left(\frac{r_c}{r_0 + r_c} \right)^2, \quad (2.31)$$

which is

$$r_c = r_0 \frac{\sqrt{6 \ln 2}}{a_0 - \sqrt{6 \ln 2}} \approx r_0 \sqrt{6 \ln 2 / a_0} = \sqrt{\frac{3 \ln 2 \sigma_0^2}{2\pi G \rho_0}}. \quad (2.32)$$

The authors reference an SIDM simulation of a Milky Way-sized halo with a resulting inner density of approximately 2.2 GeV c^{-2} cm $^{-3}$. In the dark matter dominated limit, we thus estimate the core size to be approximately 5.5 kpc, which is consistent with simulation.

For the case where neither baryons nor dark matter dominate, the authors give the following result for the core size

$$r_c \approx r_0 \frac{\sqrt{1 + \frac{2 \ln 2 a_0}{3 a_1^2}} - 1}{1 + \frac{a_0}{3 a_1} - \sqrt{1 + \frac{2 \ln 2 a_0}{3 a_1^2}}}. \quad (2.33)$$

However, we have potentially a family of solutions parameterized by a_0 and a_1 . As a criterion for consistent selection, then, the authors adopt the following convention. Let r_1 be the radius at which the average dark matter particle has undergone one interaction. We choose the values of a_0 and a_1 such that the mass and total energy within r_1 match the values that one would have had in the absence of self-interactions. To compare against “the absence of self-interactions,” one can look at, for example, an NFW profile that approximately fits the considered galaxy.

For the Milky Way, we can consider the self-interaction cross section required

for r_1 to be approximately the solar radius, 8.5 kpc. The local dark matter density is known to be approximately $0.2 \text{ GeV } c^{-2} \text{ cm}^{-3}$. We can also estimate the age of the Milky Way to be 10 Gyr. Thus, we expect the average number of scatterings to be approximately

$$(0.2 \text{ GeV } c^{-2} \text{ cm}^{-3}) (150 \text{ km/s}) (\sigma/m) (10 \text{ Gyr}). \quad (2.34)$$

A self-interaction cross section of about $\sigma/m = 1 \text{ barn/GeV}$ ($0.56 \text{ cm}^2/\text{g}$) sets this to one scattering event per particle. As we have seen, this cross section is consistent with observations on the scales of galaxies and is capable of solving the small-scale problems.

The authors specifically consider values of σ_0 , ρ_0 , and r_1 that approximate the Milky Way in the case that the no-self-interaction halo is well described by an NFW profile. They find that $r_1 = 15 \text{ kpc}$, $\sigma_0 = 165 \text{ kpc}$, $\sigma/m = 1 \text{ barn/GeV}$, and $\rho_0 = 14 \text{ GeV } c^{-2} \text{ cm}^{-3}$ gives a good fit. When plugged into Equation 2.33, this yields an expected core size of 0.43 kpc. The resulting density profiles are shown in Figure 2.1. In particular, note that the dashed red curve (SIDM analog to the standard NFW Milky Way) attains half its central density at approximately 0.5 kpc, in line with the analytic expectation.

2.4 Self-interaction in simulation

In this work, we will be exploring the introduction of self-interaction in predictions about the infall of the Sagittarius dwarf galaxy and, specifically, the formation of its stream. This is done through the use of N-body simulations. As such, we present a description of how these self-interactions are modeled in simulation. We choose to use GIZMO [59] for our simulations, and the implementation of self-interactions therein is the one described by [49]. Much of the following discussion comes in large part from [49].

In our simulation, we consider some number of “macro-particles,” each of

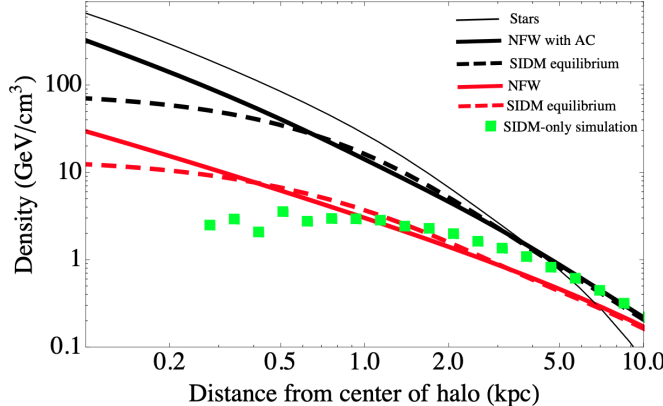


Figure 2.1: Mass density distributions for a Milky Way-sized halo. The green boxes show the result of a dark matter-only SIDM simulation. The thick solid lines show NFW distributions, both adiabatically contracted (black) and not (red). (We focus only on the non-adiabatically contracted case in this study.) The dashed lines show the corresponding analytic SIDM profiles expected from the results of the Jeans equation-based formalism. This figure is reproduced from Figure 1 of [58].

which represents an ensemble of dark matter particles, or a patch of the dark matter phase-space density. We let each macro-particle have mass m_p , and we keep this mass consistent across all dark matter macro-particles. Since we consider the macro-particle as representing a patch of the phase-space density, we consider its position to be centered at some point \mathbf{x} but spread out according to a kernel $W(r, h)$. Here, r is the distance from the center of the macro-particle and h is a smoothing length. In GADGET-2 [60], from which GIZMO is built and inherits its implementation of this algorithm, the kernel is given by

$$W(r, h) = \frac{8}{\pi h^3} \begin{cases} 1 - 6(r/h)^2 + 6(r/h)^3 & 0 \leq r/h \leq 1/2, \\ 2(1 - r/h)^3 & 1/2 < r/h \leq 1, \\ 0 & r/h > 1. \end{cases} \quad (2.35)$$

The smoothing length in GIZMO is fixed and on the order of 10 pc. The

velocity of the macro-particle is taken to instead be a delta function, such that the macro-particles have a single defined velocity.

When the patches represented by two macro-particles overlap, we can compute the interaction rate between them. The rate of scattering of a macro-particle j off a target particle i is given by

$$\Gamma(i|j) = (\sigma/m)m_p|\mathbf{v}_i - \mathbf{v}_j|g_{ji}, \quad (2.36)$$

where σ/m is the familiar cross section to mass ratio and g_{ij} is a number density factor whose purpose is account for the overlap of the two macro-particles' smoothing kernels. It is given by

$$g_{ji} = \int_0^h d^3\mathbf{x}' W(|\mathbf{x}'|, h) W(|\delta\mathbf{x}_{ji} + \mathbf{x}'|, h), \quad (2.37)$$

with $\delta\mathbf{x}_{ji}$ the displacement vector between the macro-particle positions.

Over the course of a time step δt , the probability of an interaction of macro-particle j off target macro-particle i is given by

$$P(i|j) = \Gamma(i|j) \delta t. \quad (2.38)$$

The total probability of interaction between these two particles in this time step, then, would be the average of the two directed probabilities, i.e.

$$P_{ij} = \frac{1}{2} (P(i|j) + P(j|i)). \quad (2.39)$$

To actually represent the interaction, then, one draws a random number and adjusts the velocities of the particles if the number lies below the probability. The velocities are adjusted in a manner consistent with an elastic scattering which is isotropic in the center of mass frame.

More details are presented in [49], including the derivation of the scattering

rate formula from the Boltzmann equation. We use the implementation which is packaged with the publicly-available GIZMO [59] simulation suite.

Chapter 3

Sagittarius

3.1 Overview

Sagittarius (Sgr) is a dwarf spheroidal (dSph) galaxy in the Milky Way. It was the ninth dwarf satellite discovered in the Milky Way, and the last to be discovered before the advent of digital surveys [37]. It was identified in 1994 by Ibata et al. [61] as a dwarf satellite in the constellation of Sagittarius (hence its name). The authors then noted that it was the closest galaxy to the Milky Way of any known at the time, and this has largely remained true to the present. One quirk about Sgr that was noted at the time was that it “is elongated towards the plane of the Milky Way, suggesting that it is undergoing some tidal disruption before being absorbed by the Milky Way.” This would turn out to be a very important feature of Sgr to explain.

In the years since, many studies have been performed to try to understand and quantify various properties of Sgr, like its mass, orbital time, and the reason for its elongated shape. By 2000, it was believed that the elongation was the result of tidal shearing [62], meaning that accurately describing the orbital history of Sgr is essential. Further, this means we can expect that the

stripping of stars by tidal forces may play a significant role in its evolution. Jiang and Binney [62] thus explored the parameter space for the initial mass and radius of Sgr, finding that a wide range of parameters are possible, from an initial mass of $\sim 10^{11} M_{\odot}$ and Galactocentric distance of $\gtrsim 200$ kpc to mass $\sim 10^9 M_{\odot}$ and distance ~ 60 kpc.

Shortly thereafter, Majewski et al. used the Two Micron All Sky Survey (2MASS) to map Sgr, forming the first canonical model of Sgr [63]. Their characterization of Sgr included a description of a *stream* of stars that had been tidally stripped from the progenitor, forming leading and trailing “tidal tails”. These tails, they note, “lie along a well-defined orbital plane about the Galactic center.” Moreover, they state that the lack of precession in the tidal debris is indicative of a nearly spherical gravitational potential for the Milky Way, recognizing the usefulness of the Sagittarius stream as a potential measure of the gravitational potential.

We have included a reproduction of Figure 11 from [63], a plot of a sample of Sgr debris stars in equatorial coordinates and in the orbital plane. It can be seen in Figure 3.1. The core of Sgr lies at approximately $(+20, -10)$ kpc in the orbital coordinates, with the northern arm leading above it and the southern arc leading to the left.

A similar work was performed by Belokurov et al. in 2006, using the Sloan Digital Sky Survey (SDSS) [64]. They found the tidal stream of Sgr to be “clearly visible”, and found the leading tidal arm to be especially clear. We include their Figure 2, which shows a panoramic view of the stream cutting together the 2MASS stars of Majewski et al. with the SDSS stars of Belokurov et al. This can be found in our Figure 3.2.

The picture of Sagittarius as tidally disrupted with debris forming a long streaming arc about the Milky Way would turn out to be well-supported by further observations and studies. In the ensuing years, more studies were performed to improve the model and more accurately quantify the properties

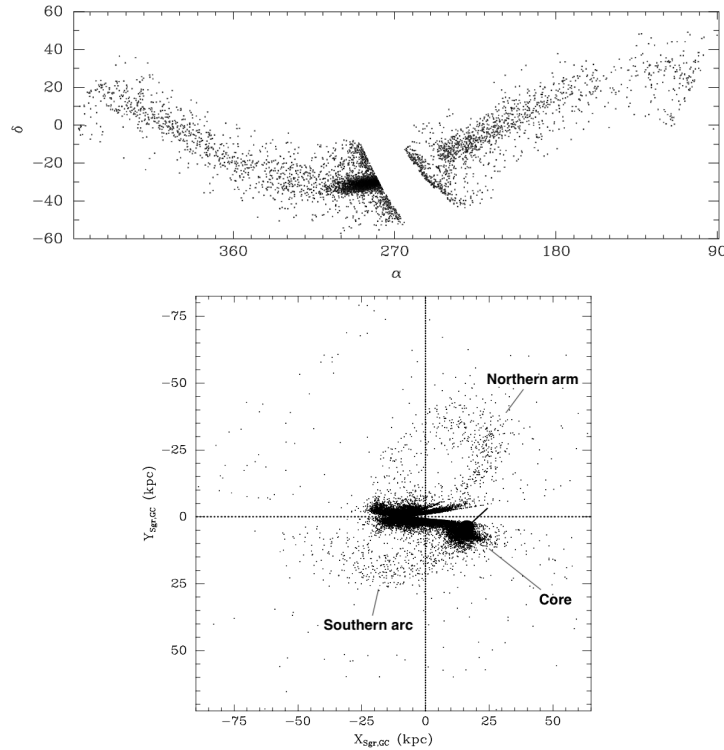


Figure 3.1: Sgr debris in (top) equatorial coordinates and (bottom) in the orbital plane with the Galactic center at the origin. Reproduced from Figures 11 and 12 of [63]; labels added to bottom figure to match their Figure 9.

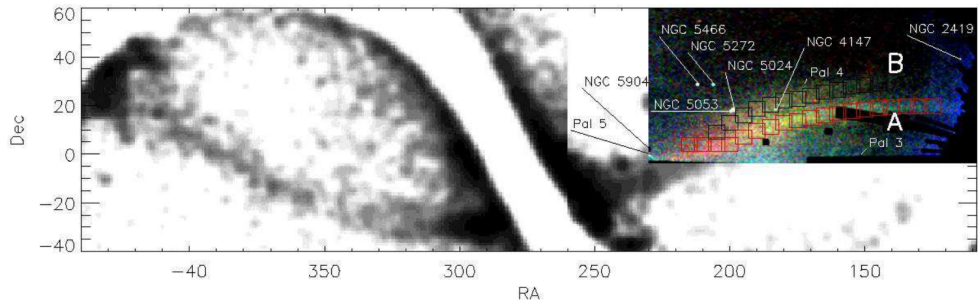


Figure 3.2: Sgr debris in equatorial coordinates, including both the 2MASS data from [63] (in grayscale) as well as SDSS data from [64] (in color). Reproduced from Figure 2 of [64].

of the galaxy. We note in particular the work of Kunder and Chaboyer [65] who estimated the distance to Sgr to be approximately 24.8 kpc.

3.2 Modern models

The next major discovery in the history of Sagittarius was the 2010 Law and Majewski model [66]. This model became the first to successfully satisfy the majority of existing constraints on the angular position, distance, and radial velocity of the tidal debris streams. It did so using a triaxial Milky Way halo; in other words, it dropped the typical assumption that the Milky Way halo is axisymmetric in the Galactic plane. One prediction of note from this model is that the current bound mass of Sgr is approximately $2.5 \times 10^8 M_\odot$. To obtain this, they use an initial mass of $6.4 \times 10^8 M_\odot$ with an infall orbit for around 8 Gyr in a fixed Galactic gravitational potential. It is worth noting that this initial mass lies in the régime where dynamical friction is small and the effects of tidal stripping on the Sgr progenitor are relatively small [67].

The resulting distribution of stars is shown in Figure 3.3. We reproduce their plots of the debris stream in terms of heliocentric coordinates and Galactocentric distances in the orbital plane. The coloring corresponds to the time at which the debris was stripped from Sgr. (Green is between the first and third apocenters, cyan between the third and fifth, magenta between the fifth and seventh, and orange later than the seventh.) Notice as well that they predict *two* wraps for both the leading (“L”) and trailing (“T”) stream arms.

Shortly thereafter came the model of Purcell et al. [68]. In their model, they explicitly account for the impact of the infall of Sagittarius on the evolution of the Milky Way disk, pointing out that all then-existing models of Sgr assume that its effects on the Galactic disk morphology are negligible. They found that Sgr created “significant perturbations to the outer disk” with

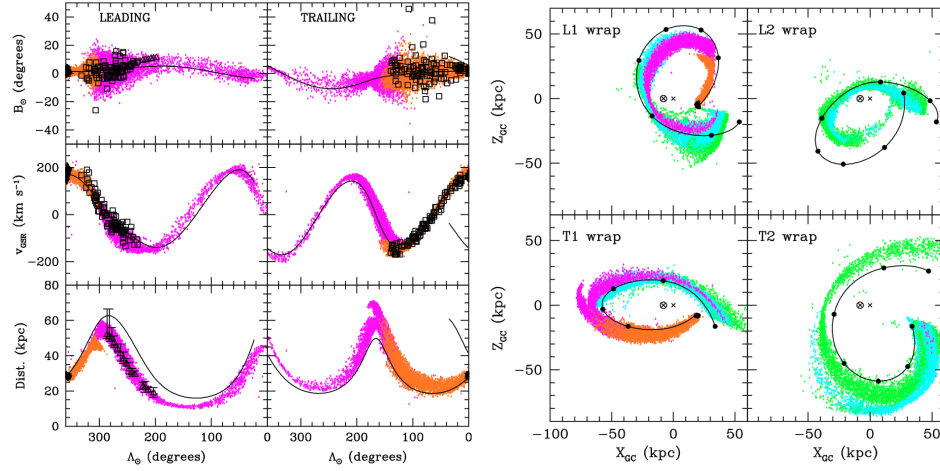


Figure 3.3: Sgr stellar debris streams according to the Law and Majewski 2010 model. On the left, debris stripped in the last ~ 3 Gyr is shown in terms of stream and heliocentric coordinates. On the right, the first two wraps of the leading (“L”) and trailing (“T”) stream arms are shown in the orbital plane. These plots are reproduced from Figures 6 and 8 of [66].

noticeable effects on the evolution of the inner spirality. In their model, Sgr is represented as beginning with halo mass $10^{10.5} M_\odot$ at a Galactocentric radius of 80 kpc in the Galactic plane. In order to account for tidal stripping that would have occurred between the infall of Sgr past the MW virial radius and the starting position they choose, they truncate the initial halo at the instantaneous Jacobi radius, $r_t = 23.2$ kpc. We note that such methods may produce qualitatively accurate representations of Sgr but are unlikely to accurately reflect the true orbital history of Sgr.

The resulting stream debris is shown in Figure 3.4. We show again both the stream in terms of heliocentric coordinates and in the orbital plane in terms of Galactocentric distances. We focus in particular on the “light Sgr” subplot of the Galactocentric figure. The figures show qualitatively similar patterns to the model of Law and Majewski [66], including the “L1” and “T1” wraps.

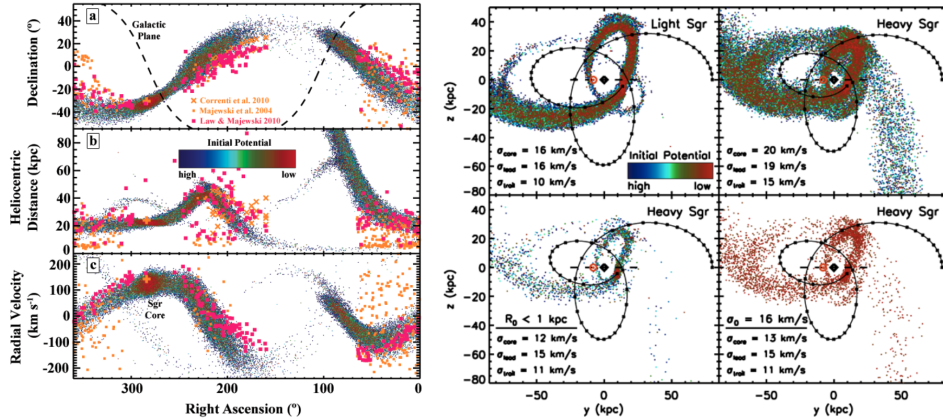


Figure 3.4: Sgr stellar debris streams according to the Purcell et al. 2011 model. On the left, debris is shown in terms of equatorial and heliocentric coordinates. On the right, the debris is shown in terms of Galactocentric distances in the orbital plane. We pay particular attention to the “light Sgr” subplot and note that the debris appears to contain approximately the same shape as the “L1” and “T1” wraps of the Law model. Figures reproduced from Figures 3 and S4 of [68].

As such, the status until quite recently was that no existing Sagittarius model could accurately account for a live Milky Way potential, the effects of dynamical friction, and the early infall of Sgr at Galactocentric radii of more than 60-80 kpc. In 2017, however, a new model which sought to solve all these problems was introduced by Dierickx and Loeb [67]. They simulated the infall of Sagittarius starting from its first crossing of the Milky Way virial radius approximately 8 Gyr ago using a live Milky Way gravitational potential and accounting for the full effects of dynamical friction. To find the best-fit model, they began by performing a parameter search with a fast and simple semi-analytic model. They then used these best-fit parameters in a full, high-resolution N-body simulation.

The resulting simulation is able to reproduce both the leading and trailing stream arms to good agreement with both observed data and past models. Moreover, they note that the resulting model is the first to accurately repro-

duce existing data for debris observed 100 kpc away. The model also predicts the existence of an extension to the stream, including “the existence of several arms of the Sgr stream extending to hundreds of kiloparsecs.” They note that this predicted structure matches the positions of the two most distant stars known in the Milky Way halo and serves as a testable prediction for data from future sky surveys.

This model is the one that we have (approximately) chosen to adopt for our simulations. The specific differences between our model and theirs will be elucidated in Section 4.1. Dierickx and Loeb represent the Milky Way halo using a Hernquist distribution with total mass $1.25 \times 10^{12} M_{\odot}$ and scale radius 38.35 kpc. The Milky Way disk follows an exponential profile with mass $8.125 \times 10^{10} M_{\odot}$, scale length 3.5 kpc, and scale height 0.525 kpc. They also use a Hernquist bulge with mass $1.25 \times 10^{10} M_{\odot}$ and scale length 0.7 kpc. In their model, Sagittarius has a Hernquist halo with total mass $1.3 \times 10^{10} M_{\odot}$ and scale radius 9.81 kpc. It has an exponential disk with mass $6 \times 10^8 M_{\odot}$, scale length 0.85 kpc, and scale height 0.1275 kpc, and a Hernquist bulge with mass $5.2 \times 10^8 M_{\odot}$ and scale length 0.17 kpc.

As before, we include plots of the resulting stellar debris, both in terms of heliocentric coordinates and Galactocentric distances in the orbital plane. These plots are given in Figure 3.5. In this case, the familiar stream structure is once again reproduced, but with the inclusion of a significant extension to the stream arms far beyond the two wraps considered by Law and Majewski. The resulting distribution also appears to approximately reproduce the distributions of observed stars (observational data shown in black).

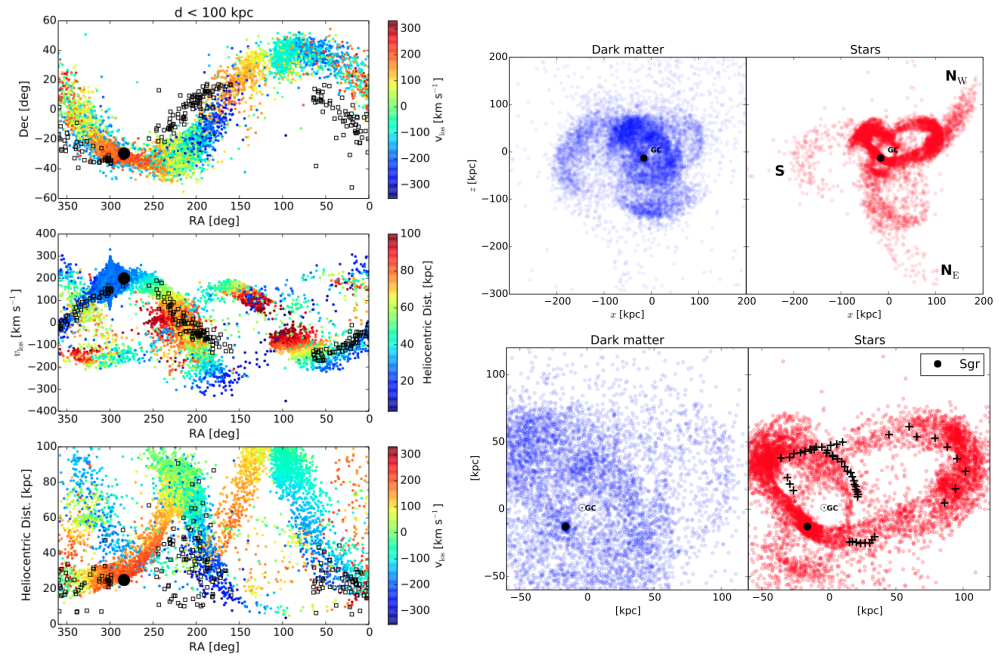


Figure 3.5: Sgr stellar debris according to the Dierickx and Loeb 2017 model. As before, we show the stream in equatorial and heliocentric coordinates on the left. On the right is the stream (and associated dark matter particles) in terms of Galactocentric distances in the orbital plane. The right top subfigure shows the full distributions, while the right bottom subfigure zooms into the more observationally relevant region. Comparisons to observed Sgr stars are also shown in black. Plots reproduced from Figures 8, 9, and 10 of [67].

Chapter 4

Simulation setup

As stated previously, the core work of this thesis is performing N-body simulations of the infall of Sgr in the style of Dierickx et al. [67], varying the initial conditions and dark matter model to determine the resulting impacts on the evolution of the Sgr tidal debris stream. As such, we provide an overview of the setup of the simulations we performed in this section.

4.1 Pipeline and parameters

To begin our experimental pipeline, we first generate the initial distributions of stellar and dark matter particles using a package called GalactICS [69]. Each galaxy is modeled using a stellar disk and dark matter halo. The halo follows a Navarro-Frenk-White (NFW) profile

$$\rho_{\text{halo}}(r) = \frac{M_{200}}{4\pi a^3 f(c)} \frac{1}{(r/a)(1+r/a)^2}, \quad (4.1)$$

where $f(c) = \log(1+c) - c/(1+c)$, M_{200} is the virial mass, a is the scale length, c is the concentration, and $c = r_{200}/a$. Here, we use a lowercase r to denote the radius in a spherical sense.

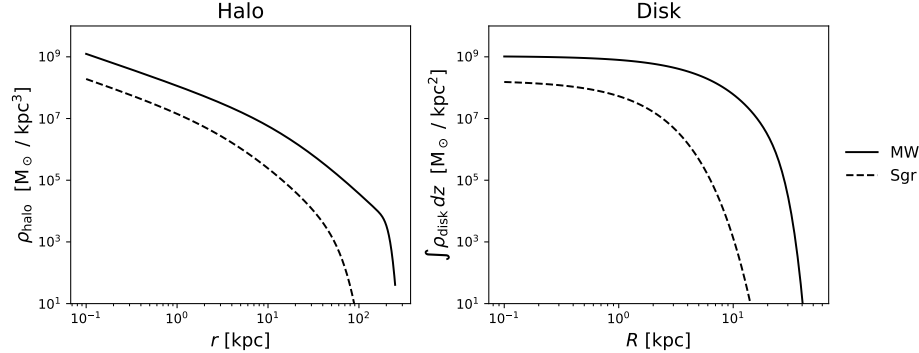


Figure 4.1: Initial profiles for the halo and disk of both galaxies. The halos follow a truncated NFW profile and the disks follow a truncated exponential-sech² profile. Note that the disk density is in cylindrical coordinates and is integrated over the z direction.

The stellar disk follows an exponential-sech² profile, given by

$$\rho_{\text{disk}}(R, z) = \frac{M_{\text{disk}}}{4\pi R_0^2 z_0} \exp(-R/R_0) \operatorname{sech}^2(z/z_0), \quad (4.2)$$

where R_0 is the disk scale length, z_0 is the disk scale height, and the capital R denotes the cylindrical radius in the plane of the disk.

Both of these distributions are subject to truncation beyond a certain radius, r_t , with truncation width dr_t . The truncation function comes from [70] and is given by

$$C(r; r_t, dr_t) = \frac{1}{2} \operatorname{erfc} \left(\frac{r - r_t}{\sqrt{2} dr_t} \right). \quad (4.3)$$

For the halos, the truncation radius is simply the virial radius and the truncation width is 20 kpc. For the disks, the truncation radius is 25 kpc, the width is 5 kpc, and the truncation is only applied to R in the disk plane. The distributions, including the truncation parameter, can be seen in Figure 4.1.

Bundled with GalactICS is a subpackage called GadgetConverters, which

Parameters	MW	Sgr
Halo		
Virial mass	M_{200}	$10^{12} M_\odot$
Virial radius	r_{200}	206 kpc
Concentration	c	10
Particles	N_{halo}	1.16×10^6
Disk		
Mass	M_{disk}	$6.5 \times 10^{10} M_\odot$
Scale length	R_0	3.5 kpc
Scale height	z_0	0.53 kpc
Particles	N_{disk}	2.03×10^6

Table 4.1: Parameters for the initial Milky Way and Sgr galaxies in our full simulation. These values are in large part taken from the work of [67].

provides a pipeline for converting the native output of GalactICS into a binary compatible with GADGET and derivative N-body simulation software. In this work, we use GIZMO [59], which is itself derived from GADGET-2 [60].

The parameters that were used for our simulations were largely taken from the work of Dierickx et al. [67]. They are summarized in Table 4.1. There are a few key differences between their model and our simulations, however. First, they used Hernquist profiles for their halos, while we use NFW distributions. The NFW parameters we use, however, come from their work, where they are given as the parameters which yield an approximately equivalent distribution. A comparison between their Hernquist and our NFW profiles is shown in Figure 4.2; the differences are quite small.

The second source of discrepancy between their work and ours is that we have less resolution in our stellar profile than in their work. This is in part because they used a Hernquist bulge in both their Milky Way and Sgr, where this has been omitted from our work. It is also because they used more stellar particles for the Sgr disk than we did (1.94×10^4 versus 1.17×10^4), owing

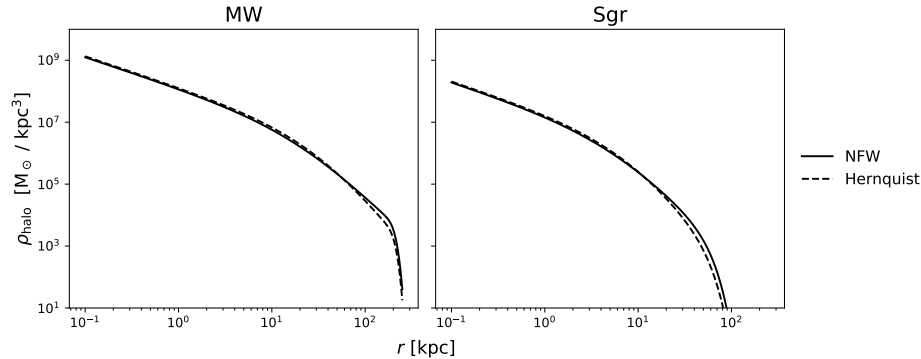


Figure 4.2: Comparison between the density distributions of the relevant truncated NFW and truncated Hernquist profiles for the Milky Way and Sgr galaxies in the Dierickx model. The NFW parameters can be found in Table 4.1. The Hernquist parameters are as follows: total MW halo mass $1.25 \times 10^{12} M_{\odot}$, MW scale radius 38.35 kpc, total Sgr halo mass $1.3 \times 10^{10} M_{\odot}$, Sgr scale radius 9.81 kpc.

to a technical error in our initial conditions creation pipeline.

The experiments performed herein were performed using GIZMO version 2020, built from commit master:0e19830, on Princeton Research Computing’s Della cluster. This cluster is an Intel cluster with ≥ 20 cores per node and ≥ 128 GB memory per node [71]. Our simulations often used around 10 GB of RAM and typically split the computation over 25 cores.

4.2 Equilibration

After generating the initial particle distributions for each galaxy, we evolved each one forward in time for several Gyrs to allow it to equilibrate. One reason we do this is because generating initial conditions which are in equilibrium is a difficult problem, and the initial conditions generator we use only gives an approximately equilibrated distribution. Evolving it forward in an isolated system allows the galaxy to come to equilibrium naturally. We have seen this to be necessary particularly for the Sgr disk distributions. Another

reason we choose to do this is to create a cored dark matter profile when using SIDM microphysics.

For each galaxy, we begin with the parameters discussed in the previous section and perform two equilibration runs: one using CDM microphysics and one using SIDM microphysics with a velocity independent cross section of $\sigma/m = 10 \text{ cm}^2/\text{g}$. In this study, we choose to use a somewhat high cross section in order to exaggerate any differences that may appear because of the presence of self-interaction. We note that future studies should consider a range of cross sections and velocity dependence.

For the Milky Way equilibrations—both CDM and SIDM—we only evolve the galaxy forward for 1 Gyr, writing time stamps approximately every 0.1 Gyr. This is because we expect the initial distribution to be relatively close to equilibrium, especially when considering such a large galaxy. The resulting evolution of the mass density profiles are shown in Figure 4.3.

In these plots, we can see that the CDM halo starts in a state which is already close to equilibrium. The halo changes very little, and the disk slowly pulls a small amount of density in toward the center. The SIDM halo, however, almost immediately develops a rather substantial core, which slowly dissolves somewhat, leaving a small core with size $\sim 1 \text{ kpc}$. This is almost certainly because of the disk. As the disk equilibrates, its central density increases, increasing the gravitational potential in the center of the galaxy and counteracting the coring effect of self-interactions.

We can also compare these results to those we might have expected following the analytic formalism for determining the core size in Section 2.3. To begin, we need to find the scale radius r_0 and the center value of the gravitational potential $\Phi_B(0)$ in the “spherical disk” approximation. We can do so by

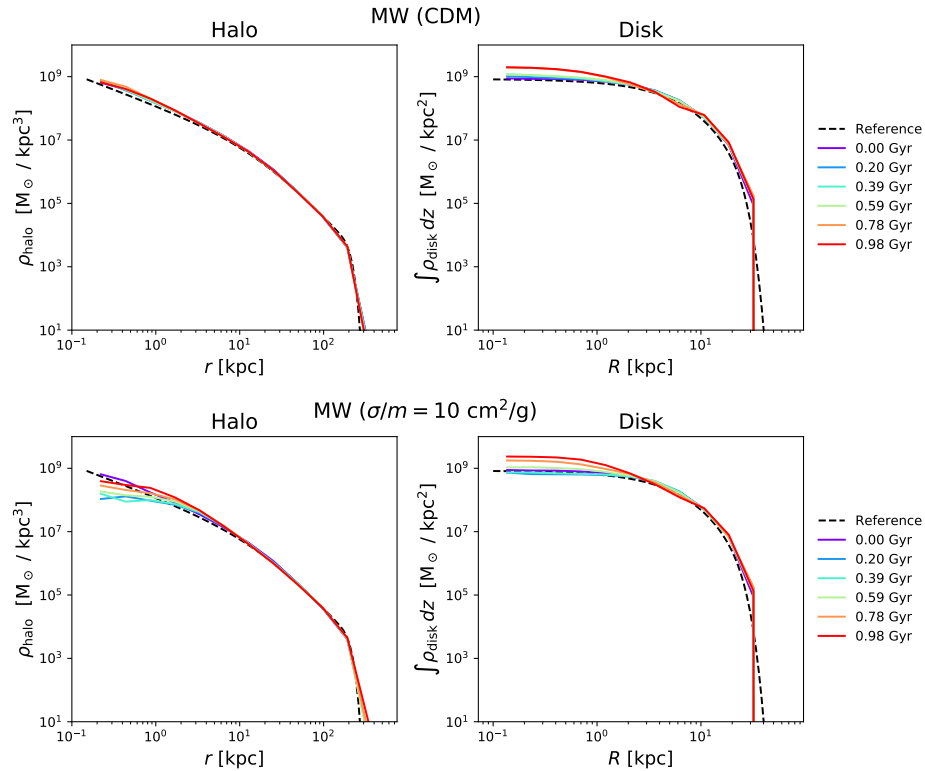


Figure 4.3: Evolution of the MW halo (left) and disk (right) during CDM (top) and SIDM ($\sigma/m = 10 \text{ cm}^2/\text{g}$) equilibration runs. The dashed line on the halo plots is the reference NFW distribution; on the disk plots it is the reference exponential-sech² distribution.

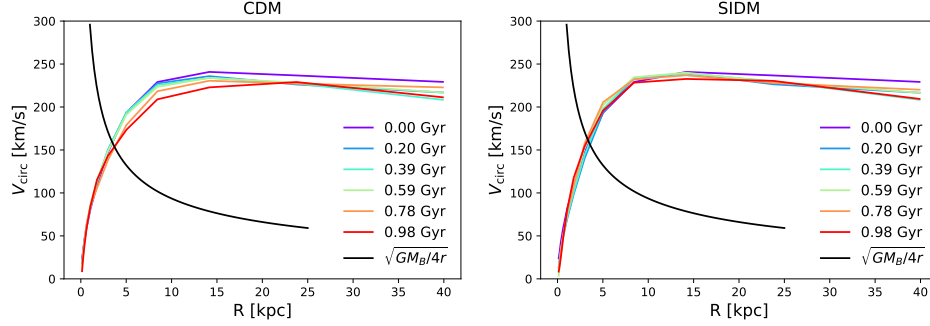


Figure 4.4: Evolution of rotation curves over time for the Milky Way disk in both the CDM and SIDM microphysics runs. Also plotted in black is $\sqrt{GM_B/4r}$, the circular velocity at the scale radius which would be expected if the disk mass followed a Hernquist profile.

using the following two relations:

$$\Phi_B(0) = -\frac{GM_B}{r_0} \quad (4.4)$$

$$V_B(r_0) = \frac{\sqrt{-\Phi_B(0)}}{2}, \quad (4.5)$$

where M_B is the mass of the baryons in the disk and V_B is the circular velocity of baryons at the given radius. Together, these imply that $V_B(r_0) = \sqrt{GM_B/4r_0}$. After truncation, our disk has a total mass of $M_B = 8.1 \times 10^{10} M_\odot$. Thus, we can plot the rotation curve of our disk and look for its intersection with $\sqrt{GM_B/4r_0}$. This should give us the values of r_0 and $V_B(r_0)$. The rotation curves for both the CDM and SIDM curves are plotted in Figure 4.4. They show $r_0 \approx 3.5$ kpc with a corresponding circular velocity $V_B(r_0) \approx 160$ km/s.

Looking back at Figure 4.3, we can estimate the central density of the halo to be $\rho_0 \approx 10^9 M_\odot/\text{kpc}^3$. We can also compute the central velocity dispersion by finding the root mean square of the radial velocities for the stars in the inner 5 kpc. For the late CDM snapshots, this measure gives $\sigma_0 = 123$ km/s.

With all these quantities, we can compute $a_0 = 43.8$ and $a_1 = 6.6$. Plugging these in to Equation 2.33, we obtain an estimate for the core size of 0.37 kpc. This core size appears to be roughly consistent with the observed core size attained in the fully evolved SIDM distribution, though perhaps a little smaller.

For the Sgr equilibrations, however, we evolved the galaxy much farther forward in time: approximately 10 Gyr for the CDM case and 20 Gyr for SIDM. These evolution times do not correspond to a physical orbit (especially given that the SIDM case would exceed the lifetime of the Universe). Rather, the initial Sgr disk distribution was found to be a bit unstable. We also wanted to be absolutely certain that the SIDM case would develop a cored profile. The evolution of the resulting Sgr mass profiles is shown in Figure 4.5.

In these plots, we see that the initial exponential-sech² distribution for the disk was not very close to equilibrium. Almost immediately, the disk redistributes itself more outwardly, with more of its mass at larger radii and a falling inner density. In the case of CDM physics, this happens within the first two Gyr, and the distribution holds relatively constant from there on. In the SIDM case, however, the distribution appears to continue to adjust, with the central density falling to around half that of the CDM disk.

In the case of the halo, we notice that the distribution holds relatively constant in the CDM case and agrees well with the reference NFW distribution. In the SIDM case, however, we see the slow development of a small core at low radii. This core appears to have a size of ≈ 1 kpc.

We can again apply the analytic expressions derived before to obtain an estimate for the expected core size. In this case, we note that the Sgr galaxy is well-approximated by the dark matter-dominated limit, so we will use the corresponding limit of the approximate core size. We again take $r_0 = 3.5$ kpc, and we estimate $\rho_0 \approx 10^{7.5} M_\odot/\text{kpc}^3$ from Figure 4.5. We again compute the central velocity dispersion by finding the root mean square of the radial

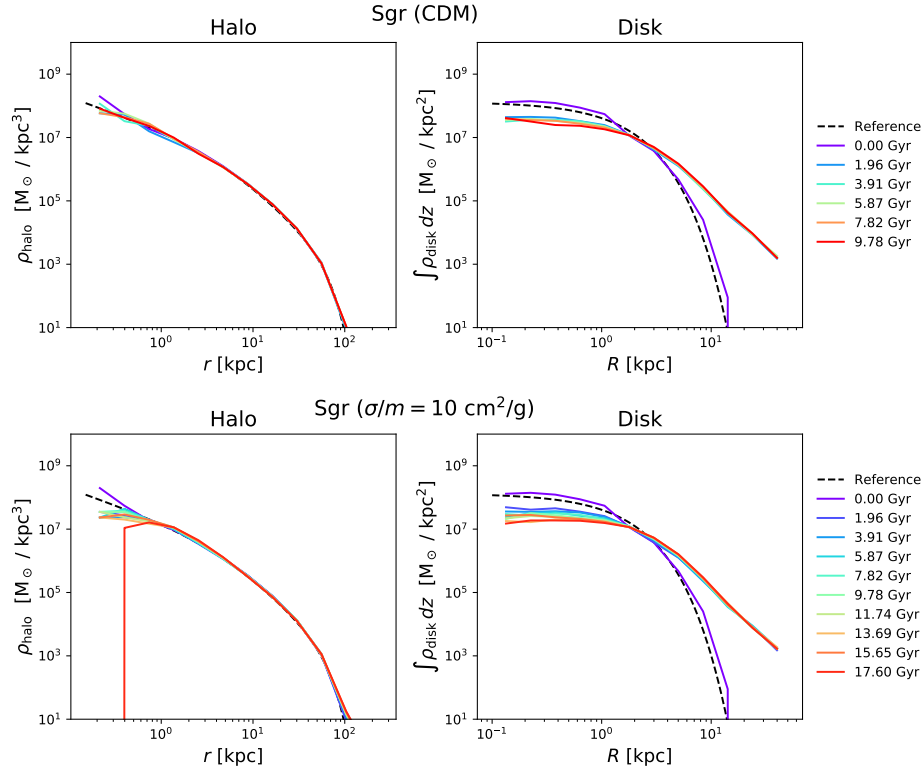


Figure 4.5: Evolution of the Sgr halo (left) and disk (right) during CDM (top) and SIDM (bottom) equilibration runs. The dashed line on the halo plots is the reference NFW distribution; on the disk plots it is the reference exponential-sech² distribution. We note in particular that the SIDM run results in generally depressed densities for both the halo and disk at low radii.

velocities for the stars in the inner 5 kpc, which in this case is $\sigma_0 = 26$ km/s. Using Equation 2.32, we obtain an estimated core size of ≈ 1.3 kpc. We find this to roughly correspond to the core seen in the final time stamp of the evolved mass density profile.

With the equilibrated MW and Sgr galaxies in both the cuspy and cored régimes, we combine them to give us two initial conditions for mergers: cuspy and cored. The Milky Way is left at its position from the equilibration run, as its center of mass will be close to the origin and its net velocity will be close to zero. Sgr is placed such that its center of mass lies at the point (125, 0, 0) kpc and is given an initial velocity $(-10, 0, 70)$ km/s. These values correspond to the best fit values found in [67].

Chapter 5

Full infall simulations

5.1 Description and initial results

With the equilibrated and merged initial conditions for both cuspy (CDM) and cored (SIDM) galaxies, we now carry out our full simulations of the Sgr infall. We will consider *three* cases: the cuspy initial conditions evolved using CDM microphysics, the cored initial conditions evolved with CDM microphysics, and the cored initial conditions evolved with SIDM microphysics. As before, we take $\sigma/m = 10 \text{ cm}^2/\text{g}$ in the SIDM case. These three mergers will be referred to as CDM/cusp, CDM/core, and SIDM respectively. By performing all three simulations, we will ideally be able to identify whether certain discrepancies between the CDM/cusp and the SIDM runs are the result of a cored initial profile or from the inclusion of self-interactions.

For each merger, the infall is simulated for 10 Gyr, with snapshots saved every 0.0978 Gyr. In Figure 5.1, we show the positions of both the stellar and dark matter particles of Sgr in the orbital plane at several times for each merger.

Even from these plots, there are some interesting patterns to note. First,

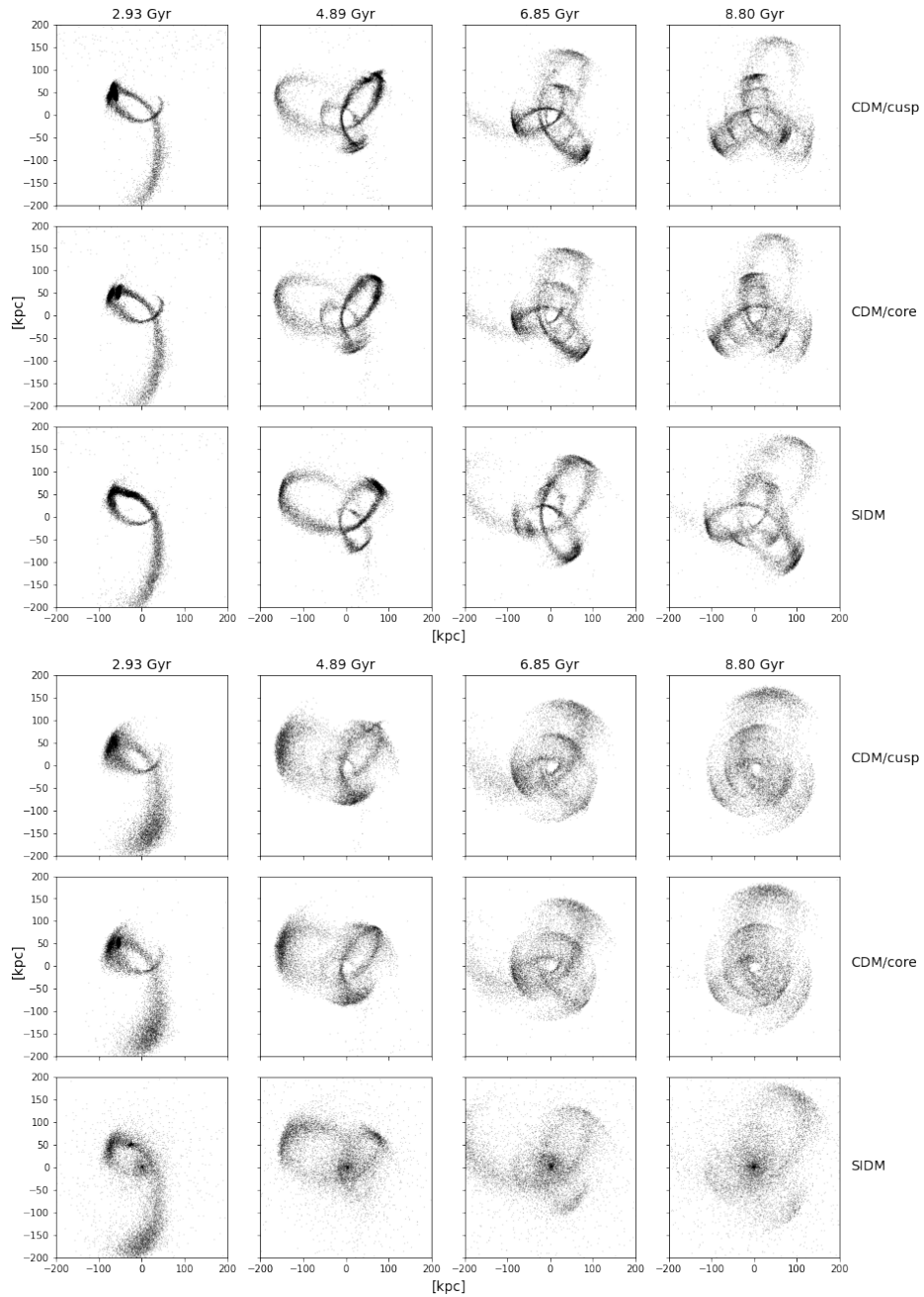


Figure 5.1: Positions of Sgr stellar (top three rows) and dark matter (bottom three rows) particles at various times for all three of the considered mergers. Each column denotes a different time; each row a different merger.

we notice the development of a winding stream structure much like that reported in [67] by around 6 to 7 Gyr in all three cases. We can also note that the CDM/core and CDM/cusp streams are rather similar, with the general shape, size, and overall rotation in agreement. There do exist some differences particularly at later times, however, particular in the inner stellar structure. For example, at 6.85 Gyr, one can see a sharply defined inner stream at (20, 60) kpc in the CDM/cusp stream which is significantly fuzzier and less dense in the CDM/core case. Similar differences emerge at the later 8.80 Gyr time stamp.

There are much more marked differences between the SIDM and CDM cases, however. The stream arms appear to be slightly rotated clockwise relative to the CDM mergers, and the general shape of the inner structure is very different. In particular, the CDM merger appear to show doubled-stream shape for the inner arms at the later time stamps which is entirely non-existent in the SIDM case. These differences are even more apparent when looking at the distribution of dark matter. In the CDM mergers, the dark matter distribution appears to roughly trace out the distribution of the stream and has a distinct hole at the origin. In the SIDM merger, however, the dark matter distribution largely loses the precise shape of the stream, instead collapsing inward toward the MW center.

We can also look at the density of particles in the orbital plane by performing a two-dimensional histogram on the data in Figure 5.1. The result is shown in Figure 5.2. The densities are integrated over the axis perpendicular to the orbital plane.

The density plots allow us to more strictly quantify some of the trends noted previously. For example, the dark matter density plots show quite concretely that the dark matter distribution in the SIDM case peaks at the Galactic center, where there is a distinct hole in the CDM mergers. The SIDM particles are also significantly less well-constrained, with a large spread extending

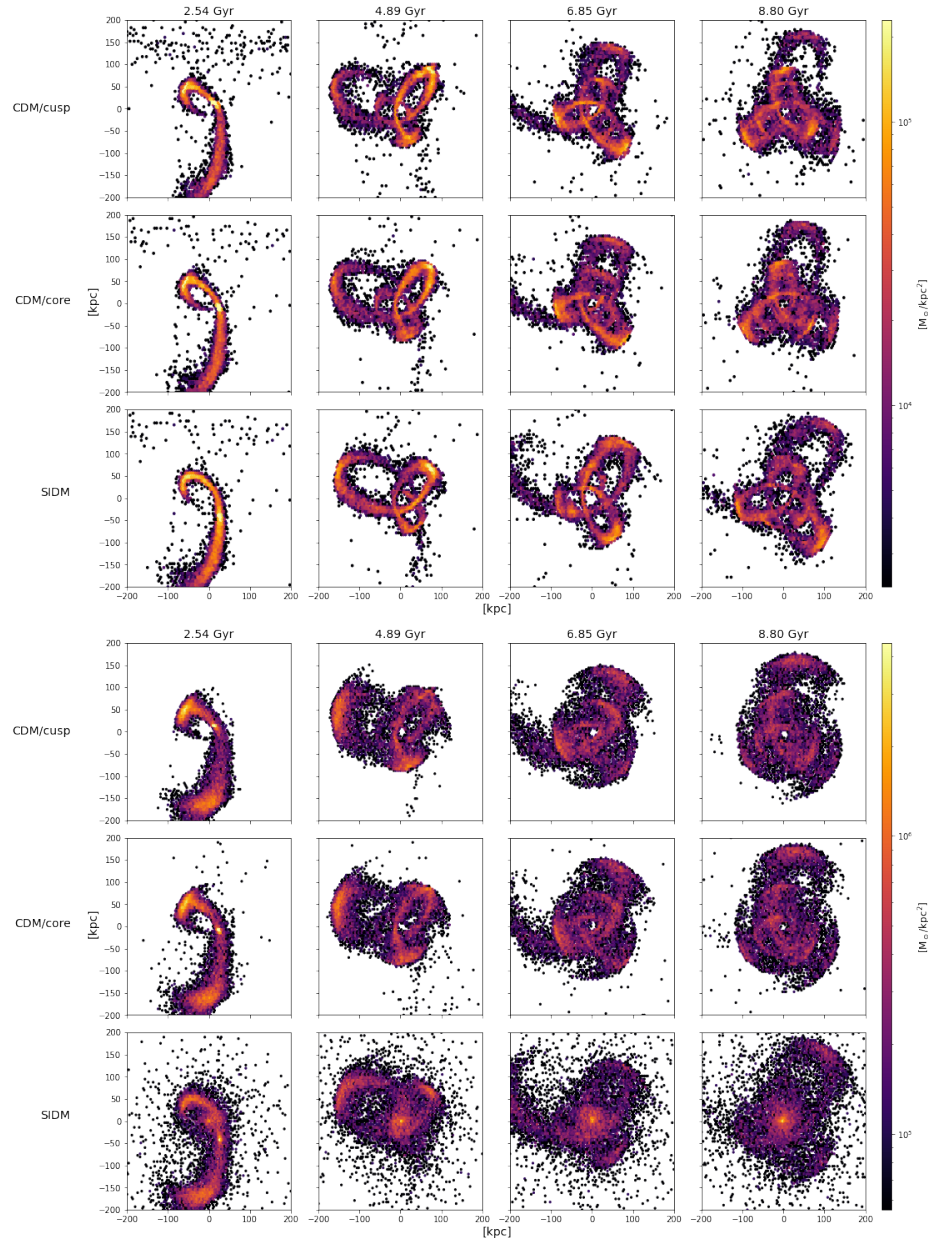


Figure 5.2: Two-dimensional density histogram of the stellar (top three rows) and dark matter (bottom three rows) Sgr particles at various times for each considered merger. Densities are integrated over the axis perpendicular to the orbital plane.

beyond the limits of the plot. This is compared to the CDM cases, where there are relatively few particles outside of the path of the stream.

Looking at the density distribution of the stellar particles allows us to quantify some of the differences noted earlier. For example, at 6.85 Gyr, the SIDM stream has a relatively high-density ($\sim 10^5 M_\odot/\text{kpc}^2$) stream arc extending from approximately $(-20, 0)$ kpc up to around $(60, 125)$ kpc. The corresponding arc exists in the CDM cases, but it is less well-defined (there is more horizontal spread) and lower density ($\sim 10^4 M_\odot/\text{kpc}^2$).

There are other, similar differences, but we would do better to analyze these differences for the specific time stamps of each merger which most closely approximate Sgr today. Determining this requires mapping the position of the Sgr progenitor, however.

5.2 Identifying the Sgr progenitor

A key part of analyzing these data is to understand the trajectory and evolution of the Sgr progenitor. As such, we desire a method for successfully identifying the position of the Sgr progenitor throughout its evolution. This is less straightforward than it may sound because of the strong effects of tidal stripping. These mean that we need to identify which particles are stripped or bound to the progenitor at any given point and omit stripped particles from our calculation of the progenitor position. In our tests, we tried a few different methods which we will describe here.

The first method that we tried was to track bound versus unbound star particles by counting particles as stripped once they exceeded a fixed radius from the center of mass of bound particles. The algorithm for this is as follows. We begin by counting the stellar particles within a certain radius on the first snapshot to be “bound”. For each snapshot after, we find the center of mass of the bound particles. Then, for each bound particle, we compute

its distance from the center of mass. If this exceeds the fixed stripping radius, we unmark the star as bound and continue.

As stated, this algorithm has two parameters that can be tuned: the initial stripping radius for the initial Sgr stellar positions and the fixed stripping radius for all following snapshots. We found it useful to describe the initial stripping radius instead in terms of the percentage of particles that are initially counted as “bound”. For example, we say that we start with the innermost 20% of particles and proceed with a fixed radius of 20 kpc. The results of applying this algorithm to the CDM/cusp merger data with a few different choices of parameters can be seen in Figure 5.3.

This figure shows us that starting with too few of the initial particles (in this case, 20%) leads to very small numbers of bound particles at late times. Further, it shows us that the trajectory of the progenitor can be somewhat sensitive to the chosen algorithm parameters, especially at late times.

This algorithm appears to have two issues that we want to try to solve. First, the actual size of the progenitor is expected to shrink with time, as progressively more of the particles are stripped. By using a fixed stripping radius, we are not modeling the expected decay of the progenitor size. The second problem we encountered is that this method appears to leave us with only $\mathcal{O}(10)$ bound particles after around 6 Gyr evolved. As such, we decided to explore modifications to the algorithm.

The first modification was to consider a decreasing stripping radius. The algorithm is very similar to before. On the first snapshot, we count some inner fraction of the particles to be “bound” and find the radius of this ball of bound particles. For the next snapshot, we strip any particles which exceed this radius (times a constant). *However*, after stripping away particles, we recompute the radius of the ball of the bound particles, and reset the stripping radius equal to this. For each snapshot following, we strip particles that are beyond this radius and recompute the radius. Over time, the

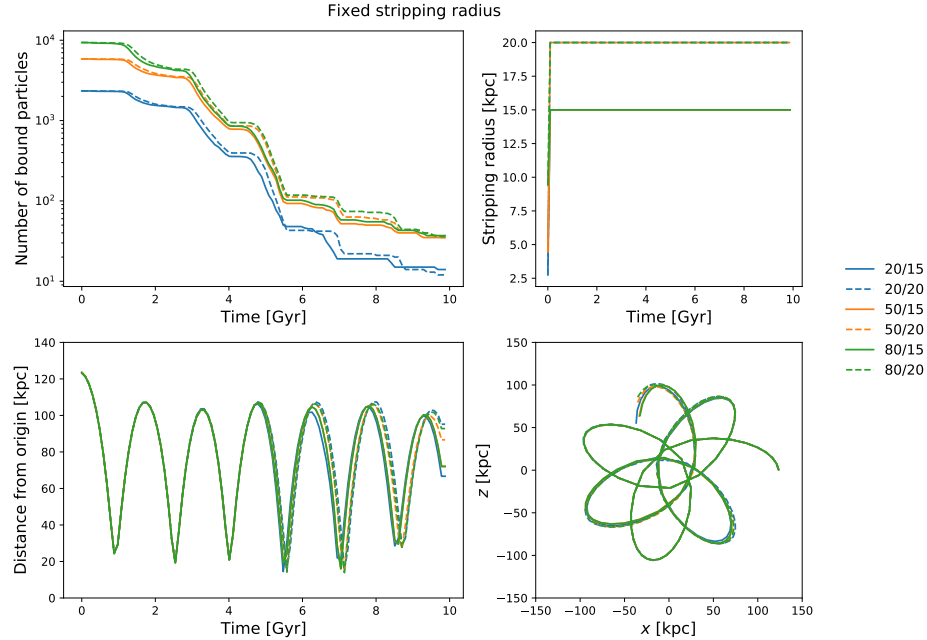


Figure 5.3: Results of applying the “fixed stripping radius” progenitor-identifying algorithm to the CDM/cusp merger data. Entries in the legend are given in the following format: “a/b” means that we started with the innermost “a”% of stellar particles and proceeded with a fixed stripping radius of “b” kpc. In the upper left is the number of bound particles over time. The upper right shows the stripping radius. The bottom left shows the distance from the origin to the Sgr center of mass; an estimate of the MW-Sgr separation. The bottom right shows the trajectory of the progenitor in the orbital plane.

stripping radius will decrease, modeling the progressively decreasing size of the progenitor. Some basic tests showed that this algorithm often becomes a bit too aggressive, so we introduced a minimum stripping radius, such that the algorithm would never use too small a stripping radius.

Further testing with a minimum stripping radius of 8 kpc and a variety of different initial parameters showed the algorithm to simply be too aggressive. For all considered combinations of parameters, we found that the algorithm reduced itself below the minimum stripping radius by around 6 Gyr. This means that at later times, when we might expect the closest resemblance to the observed Sgr progenitor, the algorithm reduces to the fixed stripping radius algorithm with a fixed radius of 8 kpc.

One possible reason that it becomes too aggressive is because the actual size of the progenitor is not monotonically decreasing. Rather, its size fluctuates over the course of the orbit, becoming quite compressed and small near the pericenter and a bit more spread out and large near the apocenter. These effects are modeled by the King formula for the tidal radius [72] as given in [67]:

$$r_t = r \left[\frac{1}{2} \frac{M_{\text{Sgr}}(< r_t)}{M_{\text{MW}}(< r)} \right]^{1/3}, \quad (5.1)$$

where $M_{\text{gal}}(< r)$ is the enclosed halo mass in galaxy “gal” within radius r of the center of mass of the galaxy, r is the distance between the Milky Way and Sgr centers of mass, and r_t is the tidal radius. For a given snapshot, then, we can compute the tidal radius according to this formula by subtracting r_t from both sides and using a simple root finder to identify the r_t which solves the equation. We then strip any particles which are farther than r_t away from the center of mass of the progenitor at the current time. Again, initial testing showed that this algorithm needed a minimum stripping radius to prevent it from stripping away all the stellar particles.

Further testing with a minimum stripping radius of 8 kpc showed this algo-

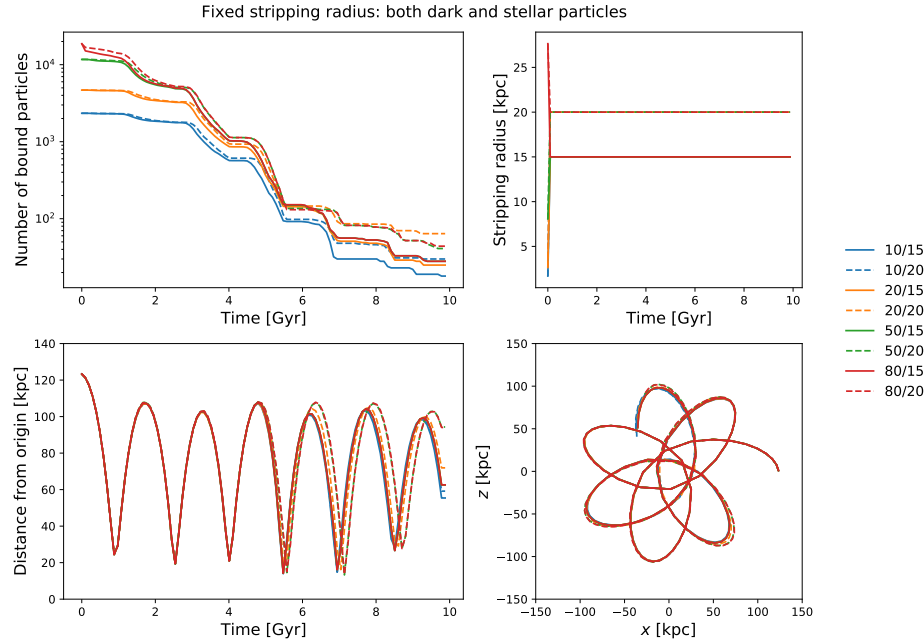


Figure 5.4: Results of using the “fixed stripping radius” progenitor-identifying algorithm on all the particles in the CDM/cusp merger data. Plots and legend entries have the same meaning as in Figure 5.3.

rithm to also be too aggressive. We tried to add a multiplicative factor to the tidal radius in order to make it a little larger before stripping, but this did not appear to help very much. After only a few Gyr, this too reduced effectively to the fixed radius strategy, using only the minimum stripping radius.

At this point, we concluded that the issue of too few bound particles at late times may be a problem related to our relatively small number of Sgr stellar particles, instead of a problem with the algorithms themselves. As such, we decided to try to use the fixed radius algorithm but using both stellar *and* dark matter particles. The result on the CDM/cusp data is shown in Figure 5.4.

This appears to yield promising results. We note that there are generally

more “bound” particles at late times when using all particles than when only using stellar ones, and that, aside from the “50/20” and “80/20” runs, the resulting trajectories appear to be more robust to the algorithm parameters. As such, we choose to move forward with this algorithm using the “20/20” parameters, as they appear to be consistent with the majority of the other parameter choices and yield the most bound particles in the end. Using these choices to identify the progenitor, we apply the algorithm to all three mergers. The resulting data are shown in Figure 5.5.

The plots in this figure are evidence that SIDM microphysics may indeed have a profound impact on the resulting trajectory of the Sgr satellite. One such difference is that the number of bound particles decreases much more substantially at early times than either of the two CDM runs. This could be explained by considering that self-interactions provide a mechanism for dark matter to free itself from shallow gravitational potential wells to which collisionless dark matter would remain confined.

Looking at the MW-Sgr separation over time, it is immediately evident that the cored profile yields a slightly longer orbital period, given the slowly increasing distance between the apo- and pericenters of the CDM/cusp and CDM/core orbits. The inclusion of self-interactions appears to add to this effect, with the CDM/cusp progenitor attaining six pericenters before the SIDM orbit is able to reach a fifth.

One phenomenon showcased by the separation curves which is difficult to understand is the lack of a consistent decay in the apocenters. We compare to Figure 6 of [67], which shows a steadily decreasing apocenter. This is the expected behavior; as the Sgr progenitor orbits and decays, we would expect it to lose energy and steadily fall inward. This, however, does not appear in our plots. In fact, this phenomenon is exacerbated in the SIDM merger, where the apocenter actually appears to *grow* after around 4 Gyr, reaching nearly 130 kpc at the 6 Gyr mark. The mechanism by which this would

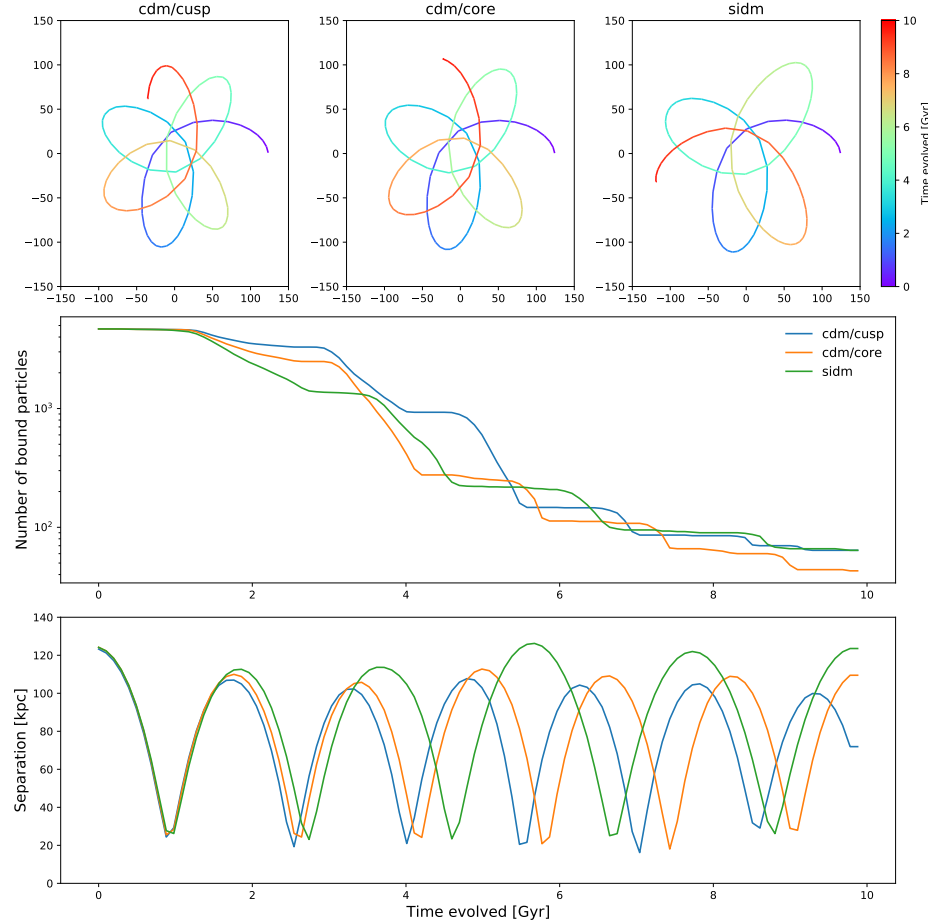


Figure 5.5: Results of using the “fixed stripping radius” progenitor-identifying algorithm on all the particles in each of the mergers. We use the “20/20” algorithm parameters for all mergers, meaning that we start with the inner 20% of particles and use a 20 kpc stripping radius. The top row shows the trajectory of the Sgr progenitor in the orbital plane for each merger. The middle row plot shows the number of bound particles over time. The bottom row plot shows the MW-Sgr separation over time.

occur is not yet understood.

Future studies would do well to explore other algorithms for identifying the Sgr progenitor, such as a friends-of-friends (FOF) halo-finder. These difficulties would also likely be alleviated by greater stellar resolution through the use of more stellar particles and the inclusion of a stellar bulge.

5.3 Comparison to stream data

5.3.1 Progenitor coordinates

As stated previously, a description of the orbit of the progenitor will allow us to determine the specific time stamps at which our mergers most closely approximate Sgr today. We take the observed coordinates of Sgr to be $(\alpha, \delta) = (283.83, -29.45)$ degrees (where α is right ascension and δ is declination) [73], proper motion $(\mu_\alpha \cos \delta, \mu_\delta) = (-2.54 \pm 0.18, -1.19 \pm 0.16)$ mas/yr [74], heliocentric distance 24.8 ± 0.8 kpc [65], and line-of-sight velocity 179 ± 1 km/s [67, 75].

To compare our data to these coordinates, we must convert from Galactocentric distances in the orbital plane to equatorial coordinates. We do this using the Astropy package [76, 77] with the assumptions that the Sun is located at approximately $(8, 0, 0)$ kpc with a velocity which is approximately directed in the positive y direction. The resulting coordinates over time are shown in Figure 5.6. We note that the right ascension data generally moves from left to right across the plot and is meant to be interpreted as wrapping around from the right edge back to the left.

We note that the Dierickx 2017 model [67] most closely approximated the observed coordinates just after its fifth pericenter, with the best agreement with the stream shape occurring then as well. Unfortunately, no snapshot of our model comes as close to these coordinates as theirs, but we believe that

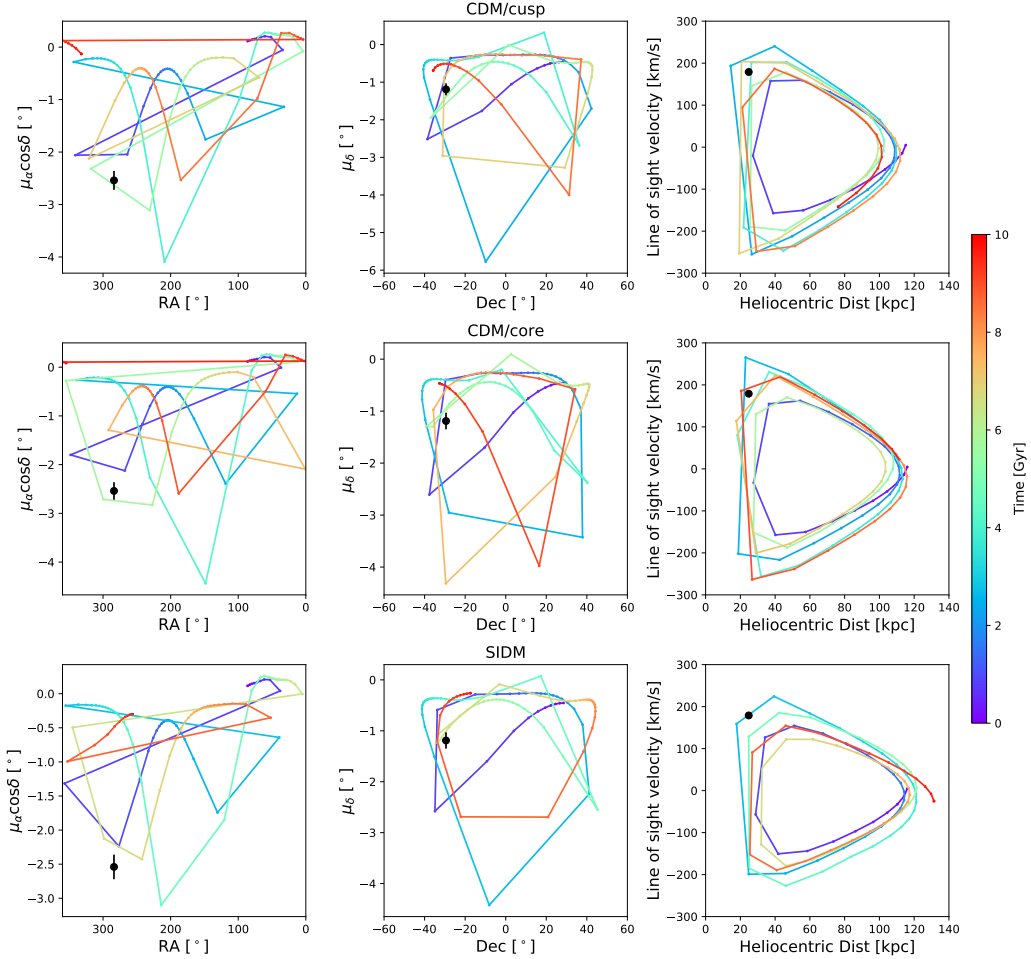


Figure 5.6: Trajectory of the Sgr progenitor in terms of equatorial coordinates and proper motions for each merger. Black squares represent the observed coordinates of the progenitor today. Error bars are present for observed quantities with uncertainties, though are in some cases smaller than the size of the marker (particularly in the velocity versus distance subplots).

this discrepancy would be alleviated somewhat by greater time resolution in the snapshots of the stream. We do, however, find that the CDM mergers attain their closest matches to the observed coordinates just after their fifth pericenters (approximately 7.04 Gyr and 7.43 Gyr for the /cusp and /core cases, respectively), in accord with the Dierickx model. The SIDM merger attains its closest match after its fourth pericenter (approximately 6.75 Gyr) with its fifth pericenter (approximately 8.80 Gyr) the next closest match.

In particular, the line-of-sight velocity versus heliocentric distance plots in the Figure show a curious trend. In the CDM cases, the trajectory passes roughly through the observed velocity and distance with every pericentric passage except the first. By contrast, no time stamp of the SIDM merger after the third pericenter appears to closely replicate the observed velocity. At such early times, however, Sgr has not completed enough wraps for the resulting stream to match existing models, such as Law 2010 or Dierickx 2017. We also note that the orbital period of the SIDM merger was seen to be significantly longer than that of either CDM merger; we believe this to be consistent with the smaller line-of-sight velocities observed here.

We can also use our progenitor-identifying algorithm to obtain estimates of the times at which each stellar particle comes unbound from the progenitor. We can thus look at the line-of-sight velocity and heliocentric distance for each star of the mergers at their respective fifth pericenters, colored according to their stripping time. Note that any particles which are still bound at the time of the snapshot are colored black. We choose to use the fifth pericenter for the SIDM merger as well because it gives the best agreement with the observed distance and line-of-sight velocity at late times, despite poorer agreement with the other dimensions. This is shown in Figure 5.7.

The resulting Figure gives a strong indication that the simulated SIDM progenitor is indeed unable to adequately reproduce the observed line-of-sight

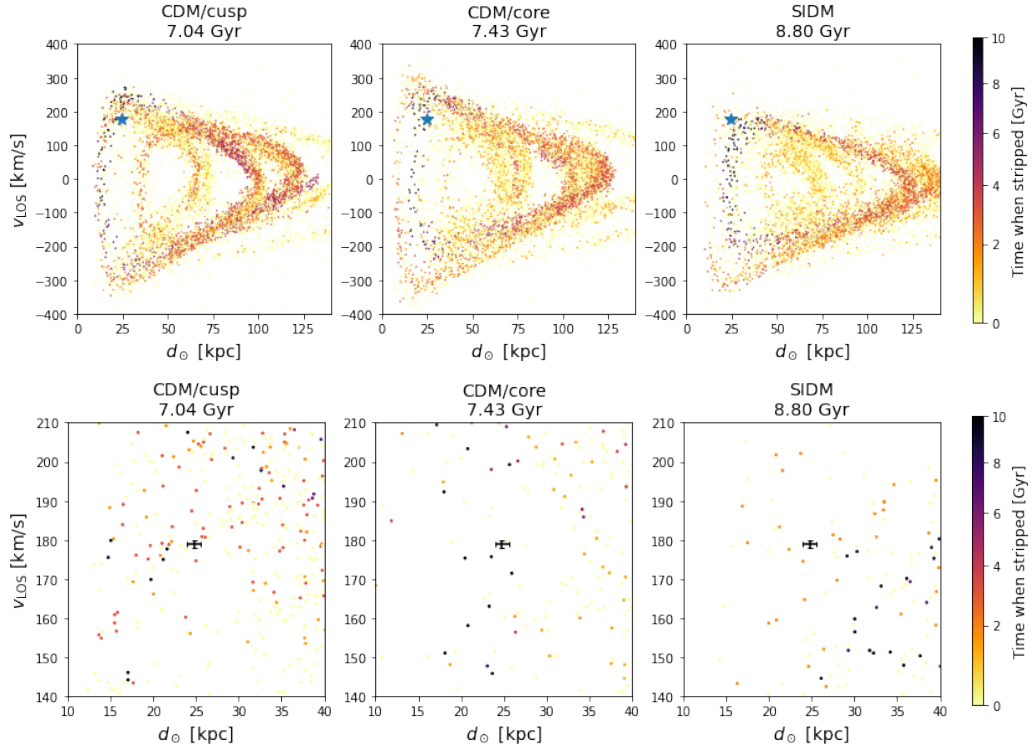


Figure 5.7: Line-of-sight velocity versus heliocentric distance for Sgr stellar particles in each merger, colored according to the time at which each particle became unbound from the progenitor. Each merger is given at its fifth pericenter. (Top) The full spread of Sgr stellar particles closer than 140 kpc, with the observed coordinates shown as a blue star. (Bottom) Only the Sgr stellar particles which are close to the observed coordinates; observed coordinates denoted by black error bars.

velocity of Sgr. In particular, we note that both CDM mergers display a number of bound (colored dark) particles which roughly surround the observed coordinates. The SIDM merger, however, shows that all bound particles either have too small a line-of-sight velocity or too large a heliocentric distance to yield the observed progenitor coordinates. We note further that this discrepancy is very significant with respect to the uncertainties in the measured coordinates.

5.3.2 Stream shape

The next piece of the analysis that we will consider is a comparison to data from the second data release (DR2) of the *Gaia* mission [78, 79], from which Sgr stars have been identified by Ibata et al. [80] using the **STREAMFINDER** (hereafter **SF**) algorithm [81, 82]. The resulting dataset includes the *Gaia* equatorial coordinates, proper motions, magnitudes, and colors of 263,438 stars, along with an estimate of the distance provided by the algorithm. They find their dataset to agree well with the Law 2010 model [66], barring a few small deviations. The **SF** sample is shown in equatorial coordinates in Figure 5.8. We note in particular a very dense region of stars at around $\alpha = 280^\circ$, $\delta = -30^\circ$, and heliocentric distance ≈ 30 kpc. This is the Sagittarius progenitor.

For each merger, we continue to consider the fifth pericenter as before. We again convert to equatorial coordinates, this time using only those stars with a heliocentric distance less than 100 kpc, as the **SF** sample contains no stars beyond this threshold. The resulting distribution of stars is plotted in Figure 5.9 with the **SF** density shown in gray.

Our comparison to the **SF** stars shows qualitatively good agreement in terms of the right ascension and declination, as the simulated streams appear to reach their maximum and minimum values of declination at the same right ascensions as the **SF** stream. We note that our streams are less thick in most

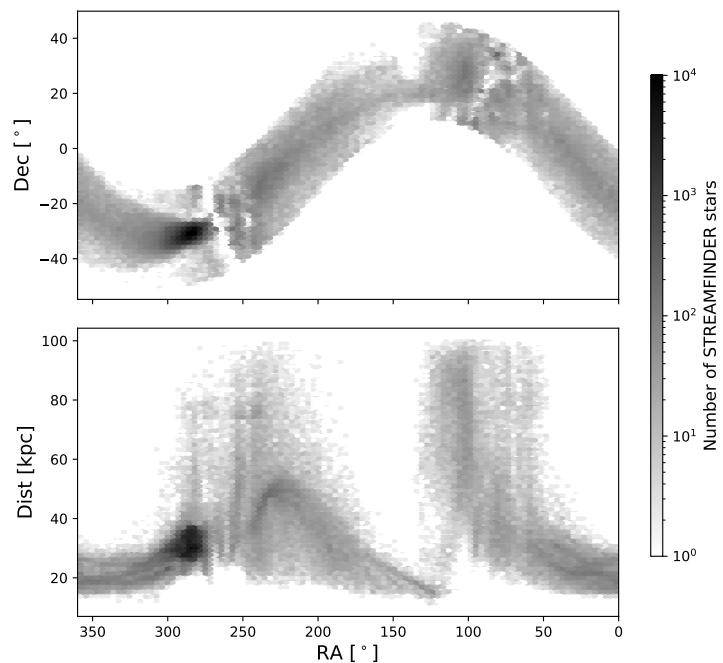


Figure 5.8: Equatorial coordinates and estimated heliocentric distances for the 263,438 Sgr stars identified by the **STREAMFINDER** algorithm.

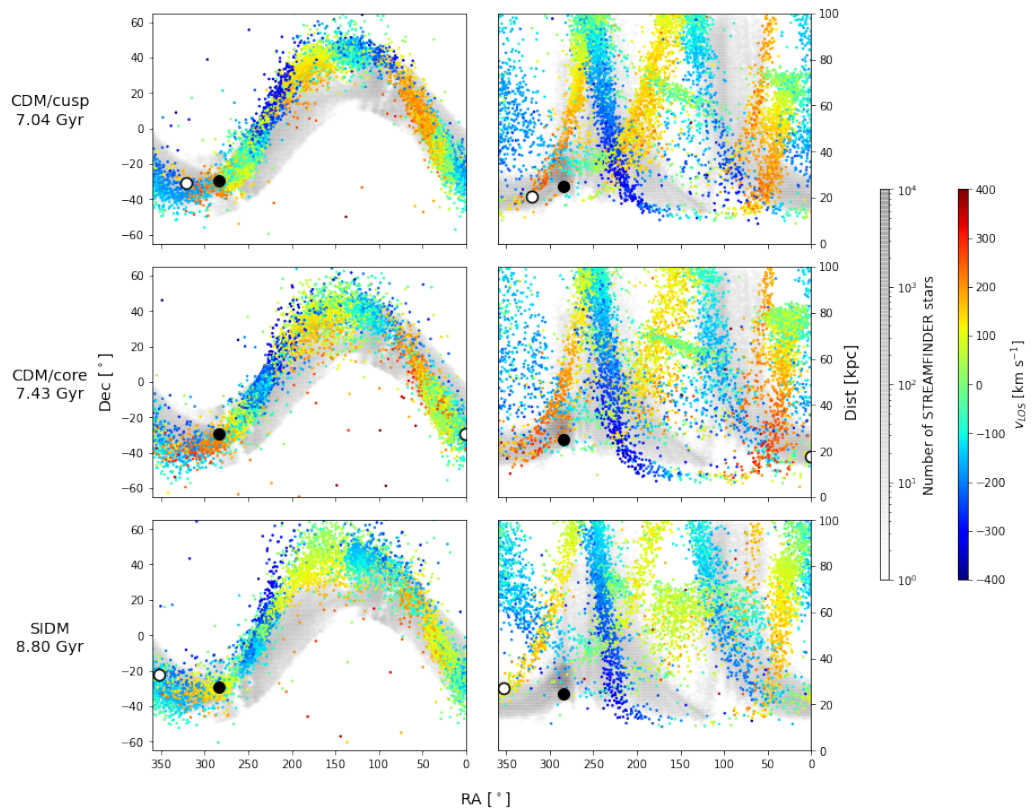


Figure 5.9: Equatorial coordinates for our simulated Sgr stellar particles of distances less than 100 kpc at the time of the fifth pericenter for each merger, colored by line-of-sight velocity. The position of the simulated progenitor is shown by a white circle with black outline. (Note that it is located at RA $\approx 0.5^\circ$ in the CDM/core plots.) The observed coordinates of Sgr are shown as a black circle. The density of STREAMFINDER stars is shown in gray.

areas, perhaps owing to a smaller number of stellar particles. Our streams also reach a greater maximum declination than the SF data; this discrepancy appears to impact the CDM/cusp merger the least and the SIDM merger the most. The SIDM merger in general appears to have larger declination values than expected from data.

When looking at the distribution of heliocentric distances, we note relatively good agreement for right ascensions larger than 200° in the CDM cases. For smaller right ascensions, we do see the reproduction of the stream arm, but shifted slightly toward larger right ascensions. This effect appears to be less present in the CDM/core case. The SIDM merger also appears to reproduce the stream arm for smaller right ascension, but is substantially less accurate at reproducing that of larger right ascensions, with the whole of the stream appearing to be shifted up by roughly 60° . The heliocentric distance distribution also shows the predicted extensions to the leading and trailing stream arms from the Dierickx model.

When plotted in these coordinates, we can also discern some differences between the mergers themselves. As an example, we can again see a marked difference in the distribution of line-of-sight velocities, as the CDM mergers both show a rather significant number of stars with large, positive line-of-sight velocities (in the orange-red region of the colormap). The SIDM merger, by contrast, has very few such stars, preferring smaller velocities. Unfortunately, the SF dataset does not come with radial velocities; as such, we choose to use another dataset for this comparison.

5.3.3 2MASS M-giants

The final comparison we will make is with M-giant stars from the Two Micron All Sky Survey (2MASS) as identified by Majewski et al. [63]. There are significantly fewer stars in this dataset (only 202), but they all include line-of-sight velocity and heliocentric distance information, allowing us to directly

compare these quantities with our simulated streams. We note further that these stars explicitly correspond to the leading and trailing stream arms of Sgr, not the progenitor.

We begin with a full comparison of our three simulated streams against the 2MASS data in terms of right ascension, declination, heliocentric distance, and line-of-sight velocity. The comparison is shown in Figure 5.10.

This Figure appears to show good agreement especially between our CDM mergers and the 2MASS data. In particular, the right ascension and declination data are almost entirely reproduced by the CDM streams, with fairly good agreement in terms of line-of-sight velocity and heliocentric distance. The SIDM stream, however, gives a much poorer reproduction of the 2MASS stream. Most prominently, at right ascensions near 200° , the corresponding declinations are all significantly greater than the 2MASS data, exactly as was seen with the SF stream.

We next compare our data to specifically the heliocentric distances and line-of-sight velocities by reproducing Figure 5.7 with the 2MASS data overlaid. The result is shown in Figure 5.11. Again, we note that still-bound particles are colored black, and unbound particles are colored according to the time when they came unbound.

This Figure again shows good general agreement between the mergers and the data. In particular, the CDM/core merger accurately reproduces many of the features of the 2MASS data at small heliocentric distances, including the distances of the closest stars. The CDM/cusp merger is the next most accurate in this region, with its closest stars being only a small amount (~ 5 kpc) farther away than given by 2MASS data. The SIDM merger again has the worst agreement of the mergers, with very few stars in the region of small heliocentric distance and low line-of-sight velocity.

These plots give more evidence to believe that the distribution of line-of-

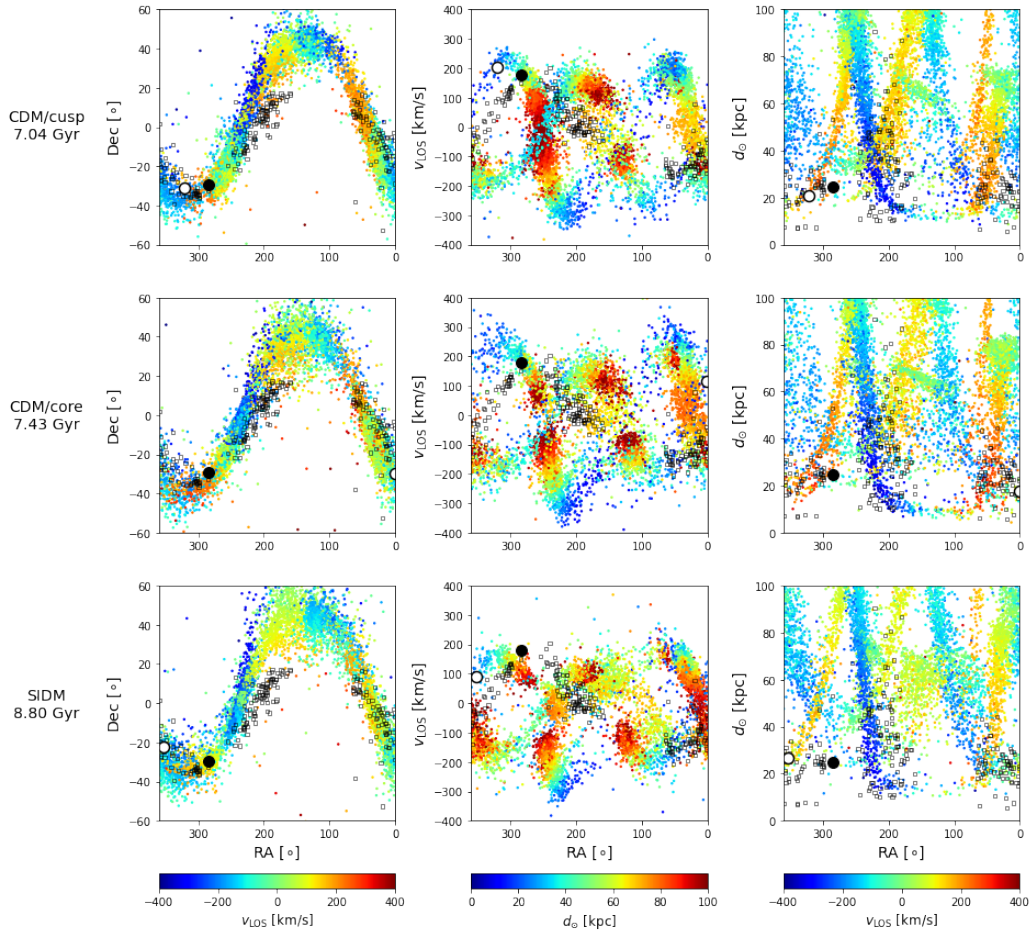


Figure 5.10: Right ascension, declination, heliocentric distance, and line-of-sight velocity for our simulated streams at their fifth pericenters. The white circle gives the position of the simulated progenitor; the black circle gives the observed coordinates of the progenitor. The black squares correspond to 2MASS M-giant stars, identified by Majewski [63].

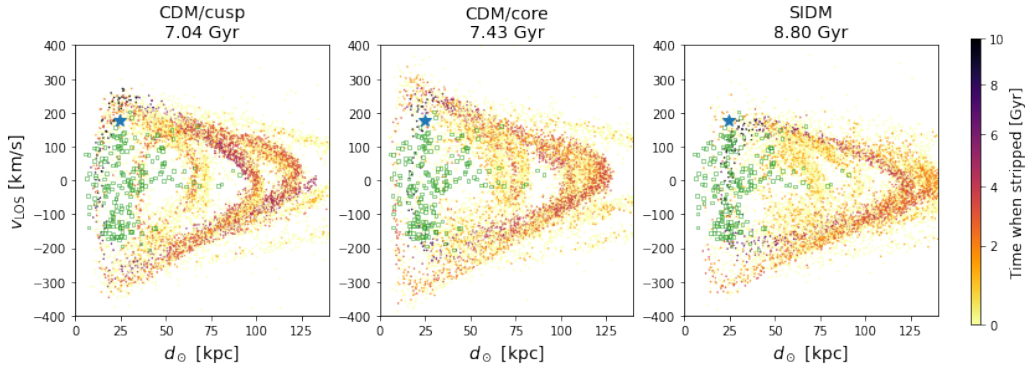


Figure 5.11: Line-of-sight velocity versus heliocentric distance for each of the three mergers at their respective fifth pericenters with particles colored according to the time they came unbound (or black if they were still bound at the considered snapshot). The blue star denotes the observed distance and velocity; the green squares denote data from 2MASS M-giant stars.

sight velocities in simulations of the Sgr stream can prove to show important differences between the CDM and SIDM dark matter models. In particular, our SIDM model appears to be significantly less able to accurately reproduce the line-of-sight velocities of the Sgr progenitor and stream.

More generally, however, we find our CDM models are able to more faithfully reproduce the observed qualities of Sgr than can our considered SIDM model. To show that this trend holds more generally of dark matter self-interaction, further studies are required. We note in particular that we have considered a rather large velocity-independent cross section ($\sigma/m = 10 \text{ cm}^2/\text{g}$) and have not varied the initial system parameters beyond what is done in the Dierickx model.

Chapter 6

Conclusions

In this work, we have presented a novel test of self-interacting dark matter models by studying simulations of the infall of the Sagittarius dwarf spheroidal galaxy. Following the Dierickx 2017 [67] model, we have performed three simulations of the infall of Sgr. Two of these used the CDM model, one using initially cuspy halos and the other using cored halos. The third used the SIDM model, starting from cored halo profiles and assuming a cross section of $\sigma/m = 10 \text{ cm}^2/\text{g}$.

In our analysis of the resulting evolutions, we found that all three develop a strong, streamlike shape. The inclusion of self-interactions, however, changes the shape dramatically, seemingly changing the overall rotation of the outer stream arms and causing the loss of the intricate inner structure seen in both CDM simulations. In general, it appears that the SIDM simulation was significantly more susceptible to the effects of tidal stripping.

Comparisons to existing Sgr data show generally good agreement especially with our CDM streams. For example, the stream shape seen in **STREAMFINDER** [80] data is reproduced quite faithfully in equatorial coordinates with similar distributions in heliocentric distance. Our mergers also show the predicted

extension to the stream introduced by the Dierickx 2017 model. The SIDM stream, while qualitatively similar to the **STREAMFINDER** shape, shows the poorest agreement of our three simulations with significantly larger declinations than expected. Similar findings were shown with a comparison to the right ascension and declination data of M-giant stars from 2MASS [63].

Moreover, the resulting SIDM progenitor is much slower than either of the CDM progenitors. Its orbital time lags significantly, with the SIDM progenitor reaching its fifth pericentric passage *after* the cuspy CDM progenitor is able to reach its sixth. This, we believe, is intimately tied to significantly smaller line-of-sight velocities at late times. The SIDM progenitor is in fact *not* able to reproduce the observed heliocentric distance and line-of-sight velocity of the Sgr progenitor at later times when the stream is sufficiently developed in our simulation. Similarly, the SIDM stream gives the least accurate reproduction of the heliocentric distance and line-of-sight velocities of the 2MASS data.

These findings suggest that line-of-sight velocity in particular may serve as an important discriminator for the existence of dark matter self-interaction. However, there are many caveats with our findings that must be more thoroughly examined in future studies. The first and most obvious is that we have only considered a single, large, velocity-independent cross section of $\sigma/m = 10 \text{ cm}^2/\text{g}$. Future studies should consider a wider range of cross sections, in particular those close to $1 \text{ cm}^2/\text{g}$, and should consider adding velocity-dependence to better match observational constraints.

The next caveat is that we have only considered initial simulation parameters (such as the initial position and velocity of Sgr) which were derived as best-fit parameters for a CDM simulation. However, the optimal description of the Sgr orbital history with SIDM likely differs from that of the CDM description. As such, the development of a semi-analytic model to explore a wider range of parameters, as was done in [67], would help to identify such parameters

and reduce any differences caused by this.

Future studies would also do well to improve the resolution of these simulations. Saving snapshots of the simulation at smaller time intervals would significantly improve the ability to match the progenitor coordinates to observation, which is currently time resolution-limited. Using more stellar particles would also likely improve the details in the resulting streams. We note further that the inclusion of a bulge in the galaxy profiles and the use of other progenitor-identifying algorithms would be greatly helpful for more accurately describing the trajectory of the simulated progenitors.

We note finally that the compilation of radial velocity data for more stars in the Sgr stream would largely improve the comparisons we make with our mergers. The **STREAMFINDER** team note that nearly 3,000 stars in their stream have radial velocity information in other public surveys; a compilation of these data would help expand the comparisons that were made at the end of this work and confirm whether the velocity distributions seen in our models are observed.

Acknowledgements

First and foremost, I would like to thank my advisor, Professor Mariangela Lisanti, for a fantastic and fulfilling year of research. This research has been incredibly exciting and interesting for me, and I always felt you left plenty of room for me to shape things how I would like. Without your guidance and advice, however, none of this would have been possible, and for that I am very grateful.

I would also like to thank the friends in my life who have helped support me in the long journey it took to get to where I am today. I would like to specifically thank my home friends—Curtis, Nate, Trumond, and Sara—for helping me to get *to* Princeton, and my Princeton friends—Alvin, Karolen, Simon, and Jason—for helping me to get *through* Princeton.

Next, I want to thank Kathryn. You have been an immense source of happiness and support to me for the past several years, and I feel you have helped me to grow a lot. Specifically, though, I want to thank you for helping me push through the rough times and to enjoy the happy ones on the other side.

Lastly, to my family: Mom, Dad, Justin, Brianna, and GJ&GJ, thank you always being there and supporting me as I took on new challenges and pushed myself to new heights. Thank you also for helping to mold me into the person I am today. I don't know what I would do without you all.

Institutional acknowledgements

This research relied heavily on NumPy¹ [83], Matplotlib² [84], and Astropy³ [76, 77], a collection of open-source Python packages for numerical computing, data visualization, and astronomy.

The simulations presented in this article were performed on computational resources managed and supported by Princeton Research Computing, a consortium of groups including the Princeton Institute for Computational Science and Engineering (PICSciE) and the Office of Information Technology’s High Performance Computing Center and Visualization Laboratory at Princeton University.

¹<https://numpy.org>

²<https://matplotlib.org>

³<https://www.astropy.org>

Bibliography

- ¹J. H. Oort, “The force exerted by the stellar system in the direction perpendicular to the galactic plane and some related problems”, Bulletin of the Astronomical Institutes of the Netherlands **6**, 249 (1932).
- ²V. Trimble, “Existence and Nature of Dark Matter in the Universe”, en, Annu. Rev. Astron. Astrophys. **25**, 425–472 (1987).
- ³F. Zwicky, “Die Rotverschiebung von extragalaktischen Nebeln”, Helvetica Physica Acta **6**, 110–127 (1933).
- ⁴H. Andernach and F. Zwicky, “English and Spanish Translation of Zwicky’s (1933) The Redshift of Extragalactic Nebulae”, arXiv:1711.01693 [astro-ph], arXiv: 1711.01693 (2017).
- ⁵H. W. Babcock, “The rotation of the Andromeda Nebula”, Lick Observatory Bulletin **19**, 41–51 (1939).
- ⁶J. H. Oort, “Some Problems Concerning the Structure and Dynamics of the Galactic System and the Elliptical Nebulae NGC 3115 and 4494.”, en, ApJ **91**, 273 (1940).
- ⁷W. Lohmann, “Die Masse der Galaxis”, de, Z. Physik **144**, 66–75 (1956).
- ⁸T. Page, “Average Masses and Mass-Luminosity Ratios of the Double Galaxies.”, The Astrophysical Journal **132**, 910–912 (1960).
- ⁹E. Holmberg, “On the masses of double galaxies”, Meddelanden fran Lunds Astronomiska Observatorium Serie I **186**, 1–20 (1954).

- ¹⁰V. Trimble, “History of Dark Matter in Galaxies”, in *Planets, Stars, and Stellar Systems: Galactic Structure and Stellar Populations*, Vol. 5, edited by T. D. Oswalt and G. Gilmore (Springer Netherlands, Dordrecht, 2013), pp. 1091–1118.
- ¹¹A. A. Penzias and R. W. Wilson, “A Measurement of Excess Antenna Temperature at 4080 Mc/s.”, *The Astrophysical Journal* **142**, 419–421 (1965).
- ¹²R. H. Dicke et al., “Cosmic Black-Body Radiation.”, *The Astrophysical Journal* **142**, 414–419 (1965).
- ¹³G. F. Smoot et al., “Structure in the COBE differential microwave radiometer first-year maps”, *The Astrophysical Journal Letters* **396**, L1–L5 (1992).
- ¹⁴G. Efstathiou, J. R. Bond, and S. D. M. White, “COBE background radiation anisotropies and large-scale structure in the universe”, *Monthly Notices of the Royal Astronomical Society* **258**, 1P–6P (1992).
- ¹⁵C. L. Bennett et al., “First-Year Wilkinson Microwave Anisotropy Probe (WMAP) Observations: Preliminary Maps and Basic Results”, *The Astrophysical Journal Supplement Series* **148**, 1–27 (2003).
- ¹⁶Planck Collaboration et al., “Planck early results. I. The Planck mission”, *Astronomy and Astrophysics* **536**, A1 (2011).
- ¹⁷V. C. Rubin and W. K. Ford Jr., “Rotation of the Andromeda Nebula from a Spectroscopic Survey of Emission Regions”, *The Astrophysical Journal* **159**, 379 (1970).
- ¹⁸M. S. Roberts and A. H. Rots, “Comparison of Rotation Curves of Different Galaxy Types”, *Astronomy and Astrophysics* **26**, 483–485 (1973).
- ¹⁹M. S. Roberts and R. N. Whitehurst, “The rotation curve and geometry of M31 at large galactocentric distances.”, *The Astrophysical Journal* **201**, 327–346 (1975).
- ²⁰J. Einasto et al., “Missing mass around galaxies: morphological evidence”, en, *Nature* **252**, Number: 5479 Publisher: Nature Publishing Group, 111–113 (1974).

- ²¹J. P. Ostriker, P. J. E. Peebles, and A. Yahil, “The size and mass of galaxies, and the mass of the universe”, *The Astrophysical Journal Letters* **193**, L1–L4 (1974).
- ²²J. P. Ostriker and P. J. E. Peebles, “A Numerical Study of the Stability of Flattened Galaxies: or, can Cold Galaxies Survive?”, *The Astrophysical Journal* **186**, 467–480 (1973).
- ²³P. Schneider, *Extragalactic Astronomy and Cosmology*, en (Springer Berlin Heidelberg, Berlin, Heidelberg, 2015).
- ²⁴A. G. Riess et al., “Observational Evidence from Supernovae for an Accelerating Universe and a Cosmological Constant”, *The Astronomical Journal* **116**, 1009–1038 (1998).
- ²⁵S. Perlmutter et al., “Measurements of Ω and Λ from 42 High-Redshift Supernovae”, *The Astrophysical Journal* **517**, 565–586 (1999).
- ²⁶S. Dodelson and F. Schmidt, *Modern Cosmology*, en, 2nd ed. (Elsevier, 2021).
- ²⁷S. Mohanty, *Astroparticle Physics and Cosmology: Perspectives in the Multimessenger Era*, en, Vol. 975, Lecture Notes in Physics (Springer International Publishing, Cham, 2020).
- ²⁸L. Bergström and A. Goobar, *Cosmology and particle astrophysics*, en, 2. ed., reprinted, Springer Praxis books in astronomy and planetary science, OCLC: 254584818 (Springer, Berlin, 2008).
- ²⁹J. S. Bullock and M. Boylan-Kolchin, “Small-Scale Challenges to the Λ CDM Paradigm”, *Annual Review of Astronomy and Astrophysics* **55**, 343–387 (2017).
- ³⁰C. S. Frenk et al., “The formation of dark halos in a universe dominated by cold dark matter”, *The Astrophysical Journal* **327**, 507–525 (1988).
- ³¹J. Dubinski and R. G. Carlberg, “The structure of cold dark matter halos”, *The Astrophysical Journal* **378**, 496–503 (1991).
- ³²J. F. Navarro, C. S. Frenk, and S. D. M. White, “The Structure of Cold Dark Matter Halos”, arXiv:astro-ph/9508025, arXiv: astro-ph/9508025 (1995).

- ³³J. Binney and S. Tremaine, *Galactic dynamics*, 2nd ed, Princeton series in astrophysics (Princeton University Press, Princeton, 2008).
- ³⁴L. Hernquist, “An analytical model for spherical galaxies and bulges”, *The Astrophysical Journal* **356**, 359–364 (1990).
- ³⁵J. F. Navarro, C. S. Frenk, and S. D. M. White, “A Universal Density Profile from Hierarchical Clustering”, arXiv:astro-ph/9611107, arXiv: astro-ph/9611107 (1997).
- ³⁶R. Flores et al., “Rotation curves from baryonic infall - Dependence on disk-to-halo ratio, initial angular momentum, and core radius, and comparison with data”, *The Astrophysical Journal* **412**, 443–454 (1993).
- ³⁷J. D. Simon, “The Faintest Dwarf Galaxies”, *Annual Review of Astronomy and Astrophysics* **57**, 375–415 (2019).
- ³⁸M. Boylan-Kolchin, J. S. Bullock, and M. Kaplinghat, “Too big to fail? The puzzling darkness of massive Milky Way subhaloes”, *Monthly Notices of the Royal Astronomical Society* **415**, L40–L44 (2011).
- ³⁹A. Pontzen and F. Governato, “How supernova feedback turns dark matter cusps into cores”, *Monthly Notices of the Royal Astronomical Society* **421**, 3464–3471 (2012).
- ⁴⁰T. K. Chan et al., “The impact of baryonic physics on the structure of dark matter haloes: the view from the FIRE cosmological simulations”, *Monthly Notices of the Royal Astronomical Society* **454**, 2981–3001 (2015).
- ⁴¹D. N. Spergel and P. J. Steinhardt, “Observational Evidence for Self-Interacting Cold Dark Matter”, *Physical Review Letters* **84**, 3760–3763 (2000).
- ⁴²A. Burkert, “The Structure and Evolution of Weakly Self-interacting Cold Dark Matter Halos”, *The Astrophysical Journal Letters* **534**, L143–L146 (2000).
- ⁴³R. Davé et al., “Halo Properties in Cosmological Simulations of Self-interacting Cold Dark Matter”, *The Astrophysical Journal* **547**, 574–589 (2001).
- ⁴⁴B. Moore et al., “Collisional versus Collisionless Dark Matter”, *The Astrophysical Journal Letters* **535**, L21–L24 (2000).

- ⁴⁵N. Yoshida et al., “Collisional Dark Matter and the Structure of Dark Halos”, *The Astrophysical Journal Letters* **535**, L103–L106 (2000).
- ⁴⁶N. Yoshida et al., “Weakly Self-interacting Dark Matter and the Structure of Dark Halos”, *The Astrophysical Journal Letters* **544**, L87–L90 (2000).
- ⁴⁷M. Meneghetti et al., “Giant cluster arcs as a constraint on the scattering cross-section of dark matter”, *Monthly Notices of the Royal Astronomical Society* **325**, 435–442 (2001).
- ⁴⁸J. Miralda-Escudé, “A Test of the Collisional Dark Matter Hypothesis from Cluster Lensing”, *The Astrophysical Journal* **564**, 60–64 (2002).
- ⁴⁹M. Rocha et al., “Cosmological simulations with self-interacting dark matter - I. Constant-density cores and substructure”, *Monthly Notices of the Royal Astronomical Society* **430**, 81–104 (2013).
- ⁵⁰A. H. G. Peter et al., “Cosmological simulations with self-interacting dark matter - II. Halo shapes versus observations”, *Monthly Notices of the Royal Astronomical Society* **430**, 105–120 (2013).
- ⁵¹J. Zavala, M. Vogelsberger, and M. G. Walker, “Constraining self-interacting dark matter with the Milky Way’s dwarf spheroidals”, *Monthly Notices of the Royal Astronomical Society* **431**, L20–L24 (2013).
- ⁵²O. D. Elbert et al., “Core formation in dwarf haloes with self-interacting dark matter: no fine-tuning necessary”, *Monthly Notices of the Royal Astronomical Society* **453**, 29–37 (2015).
- ⁵³S. Tulin and H.-B. Yu, “Dark matter self-interactions and small scale structure”, *Physics Reports* **730**, 1–57 (2018).
- ⁵⁴S. Tulin, H.-B. Yu, and K. M. Zurek, “Beyond Collisionless Dark Matter: Particle Physics Dynamics for Dark Matter Halo Structure”, *Phys. Rev. D* **87**, arXiv: 1302.3898, 115007 (2013).
- ⁵⁵S. Tulin, H.-B. Yu, and K. M. Zurek, “Resonant Dark Forces and Small Scale Structure”, *Phys. Rev. Lett.* **110**, arXiv: 1210.0900, 111301 (2013).

- ⁵⁶G. D. Kribs and E. T. Neil, “Review of strongly-coupled composite dark matter models and lattice simulations”, *Int. J. Mod. Phys. A* **31**, arXiv: 1604.04627, 1643004 (2016).
- ⁵⁷J. M. Cline et al., “Composite strongly interacting dark matter”, *Phys. Rev. D* **90**, arXiv: 1312.3325, 015023 (2014).
- ⁵⁸M. Kaplinghat et al., “Tying Dark Matter to Baryons with Self-Interactions”, *Physical Review Letters* **113**, 021302 (2014).
- ⁵⁹P. F. Hopkins, “A new class of accurate, mesh-free hydrodynamic simulation methods”, *Monthly Notices of the Royal Astronomical Society* **450**, 53–110 (2015).
- ⁶⁰V. Springel, “The cosmological simulation code GADGET-2”, *Monthly Notices of the Royal Astronomical Society* **364**, arXiv: astro-ph/0505010, 1105–1134 (2005).
- ⁶¹R. A. Ibata, G. Gilmore, and M. J. Irwin, “A dwarf satellite galaxy in Sagittarius”, en, *Nature* **370**, Number: 6486 Publisher: Nature Publishing Group, 194–196 (1994).
- ⁶²I.-G. Jiang and J. Binney, “The orbit and mass of the Sagittarius dwarf galaxy”, *Monthly Notices of the Royal Astronomical Society* **314**, 468–474 (2000).
- ⁶³S. R. Majewski et al., “A Two Micron All Sky Survey View of the Sagittarius Dwarf Galaxy. I. Morphology of the Sagittarius Core and Tidal Arms”, *The Astrophysical Journal* **599**, 1082–1115 (2003).
- ⁶⁴V. Belokurov et al., “The Field of Streams: Sagittarius and Its Siblings”, *The Astrophysical Journal Letters* **642**, L137–L140 (2006).
- ⁶⁵A. Kunder and B. Chaboyer, “Distance to the Sagittarius Dwarf Galaxy Using Macho Project RR Lyrae Stars”, *The Astronomical Journal* **137**, 4478–4486 (2009).
- ⁶⁶D. R. Law and S. R. Majewski, “The Sagittarius Dwarf Galaxy: A Model for Evolution in a Triaxial Milky Way Halo”, *The Astrophysical Journal* **714**, 229–254 (2010).

- ⁶⁷M. Dierickx and A. Loeb, “Predicted Extension of the Sagittarius Stream to the Milky Way Virial Radius”, *ApJ* **836**, arXiv: 1611.00089, 92 (2017).
- ⁶⁸C. W. Purcell et al., “The Sagittarius impact as an architect of spirality and outer rings in the Milky Way”, *Nature* **477**, 301–303 (2011).
- ⁶⁹N. Deg et al., “GalactICS with Gas”, *Monthly Notices of the Royal Astronomical Society* **486**, arXiv: 1904.12700, 5391–5399 (2019).
- ⁷⁰L. M. Widrow, B. Pym, and J. Dubinski, “Dynamical Blueprints for Galaxies”, *ApJ* **679**, arXiv: 0801.3414, 1239–1259 (2008).
- ⁷¹Princeton Research Computing, *Della*, en.
- ⁷²I. King, “The structure of star clusters. I. an empirical density law”, *The Astronomical Journal* **67**, 471 (1962).
- ⁷³NASA and California Institute of Technology, *NASA/IPAC Extragalactic Database: Sagittarius Dwarf Spheroidal*.
- ⁷⁴D. Massari et al., “Hubble Space Telescope Absolute Proper Motions of NGC 6681 (M70) and the Sagittarius Dwarf Spheroidal Galaxy”, *ApJ* **779**, 81 (2013).
- ⁷⁵M. Bellazzini et al., “The Nucleus of the Sagittarius dSph Galaxy and M54: A Window on the Process of Galaxy Nucleation”, *The Astronomical Journal* **136**, 1147–1170 (2008).
- ⁷⁶Astropy Collaboration et al., “Astropy: A community Python package for astronomy”, *Astronomy and Astrophysics* **558**, A33 (2013).
- ⁷⁷Astropy Collaboration et al., “The Astropy Project: Building an Open-science Project and Status of the v2.0 Core Package”, *The Astronomical Journal* **156**, 123 (2018).
- ⁷⁸L. Lindegren et al., “Gaia Data Release 2. The astrometric solution”, *Astronomy and Astrophysics* **616**, A2 (2018).
- ⁷⁹Gaia Collaboration et al., “Gaia Data Release 2. Summary of the contents and survey properties”, *Astronomy and Astrophysics* **616**, A1 (2018).

- ⁸⁰R. Ibata et al., “A Panoramic Landscape of the Sagittarius Stream in Gaia DR2 Revealed with the STREAMFINDER Spyglass”, *The Astrophysical Journal Letters* **891**, L19 (2020).
- ⁸¹K. Malhan and R. A. Ibata, “STREAMFINDER – I. A new algorithm for detecting stellar streams”, *Monthly Notices of the Royal Astronomical Society* **477**, 4063–4076 (2018).
- ⁸²K. Malhan, R. A. Ibata, and N. F. Martin, “Ghostly tributaries to the Milky Way: charting the halo’s stellar streams with the Gaia DR2 catalogue”, *Monthly Notices of the Royal Astronomical Society* **481**, 3442–3455 (2018).
- ⁸³C. R. Harris et al., “Array Programming with NumPy”, *arXiv e-prints* **2006**, arXiv:2006.10256 (2020).
- ⁸⁴J. D. Hunter, “Matplotlib: A 2D Graphics Environment”, *Computing in Science and Engineering* **9**, 90–95 (2007).